Saddle-node bifurcations of traveling waves in the asymptotic suction boundary layer flow

H. Wedin[1] and S. Cherubini[2,*]

[1]*Department of Civil, Chemical and Environmental Engineering, University of Genova, Via Montallegro 1, 16145 Genova, Italy*

[2]*Dipartimento di Meccanica, Matematica e Management, Politecnico di Bari, Via Re David 200, 70125 Bari, Italy*

(Received 15 February 2019; published 15 October 2019)

This work aims at investigating three-dimensional finite-amplitude traveling wave solutions of the asymptotic suction boundary layer, as well as their role in state space, based on direct numerical simulations. Using a body forcing and allowing wall-normal perturbations at the wall to be nonzero and linked to the pressure gradient through a wall permeability a, nonlinear invariant solutions of the Navier-Stokes equations are found and continued towards low values of the Reynolds number. The solutions, having a reflect symmetry in the spanwise coordinate, set a new threshold in state space for the onset of exact coherent flow structures. The obtained traveling waves emerge from a saddle-node bifurcation at $\mathrm{Re}_{SN} = 225$ (based on the displacement thickness) for vanishing wall permeability. Increasing a to small but finite values changes but slightly the value of Re_{SN}. In all cases, the obtained Re_{SN} is below the lowest Reynolds number at which sustained turbulence is observed, namely, $\mathrm{Re} \approx 270$ according to recent works. The corresponding waves in the Blasius boundary layer flow without suction exist from $\mathrm{Re}_{SN} = 496$, meaning that the asymptotic suction boundary layer might be more nonlinearly unstable (although more linearly stable) than the Blasius one. In the interval of Re studied it is found that the traveling waves occupy a region extending from the wall to the log-law region, with maximum root-mean-square velocities approaching those obtained by direct numerical simulations in the turbulent regime, especially for nonvanishing permeability. These solutions are found to be unstable, with steady leading modes, whose growth rate increases with the permeability and with the Reynolds number. When the trajectory escapes from these traveling waves along their unstable directions, transition to turbulence is observed even at Reynolds number as low as $\mathrm{Re} = 240$, suggesting that these solutions may play an important role in turbulent transition at low Reynolds numbers.

DOI: 10.1103/PhysRevFluids.4.104401

I. INTRODUCTION

The key to a complete understanding of turbulent flows still eludes the scientific community. The study of transition to turbulence saw its beginning with the well-known experimental study of Osborne Reynolds in 1883 on the circular pipe flow configuration [1]. Reynolds observed that, at sufficiently low flow speeds, the fluid remained laminar, whereas at increasing speed the flow began to oscillate before turning turbulent downstream. Ever since, the problem of understanding the mechanism behind transition to turbulence has fascinated thousands of scientists, who tackled it using experimental approaches or various theoretical or numerical ways to simulate

*s.cherubini@gmail.com

the flow and analyze its dynamics. The first theoretical approaches used to attempt unraveling this problem were those of linear stability analysis, at first in the inviscid case [2] providing the famous Rayleigh's inflection point criterion, and then in the viscous case [3,4], allowing one to find unstable Tollmien-Schiliching waves arising in boundary layer and channel flows when the Reynolds number overtakes a critical value. However, in many cases transition to turbulence occurs subcritically, for Reynolds numbers much lower than the critical value, making the linear stability approaches not suited for predicting and analyzing laminar-turbulent transition. Weakly nonlinear expansions were also attempted, which account for the nonlinear interactions between different wave numbers [5], allowing to obtain bifurcation diagrams in both supercritical and subcritical conditions. However, these analytical methods are able to treat only simple cases in which the perturbations are characterized by no more than two or three wave numbers, whereas in realistic conditions disturbances show a much richer spectrum. Crucial contributions in this field came from Hopf [6], who used the dynamical system theory introduced by Poincaré [7] to show how transition to turbulence can be modeled by the dynamics in state space of simplified model equations. Subsequently, the importance of unstable periodic orbits for describing chaos was demonstrated in Ref. [8], initiating the dynamical system description of chaos and turbulence. Because of these seminal works, the turbulent dynamics in fluids can be viewed as a dynamical system built up by invariant solutions occupying the state space, having the form of unstable periodic orbits or (rather simple) steady states and traveling waves [9–18]. These solutions behave as saddle points in the state space, making up the skeleton of the invariant set of flow states of the Navier-Stokes equations. A typical trajectory of the fluid motion wanders repeatedly in a succession of close approaches to these and other flow states [19,20]. Stepping up in the hierachy of invariant flow solutions one finds more complicated unstable periodic or chaotic states such as edge states sitting on the laminar-turbulent boundary (the edge of chaos) or other types of periodic solutions extracted from numerical simulations, which might be localized or not in space [21–30]. Although traveling-wave solutions cannot provide a reliable estimate of dynamical averages, several studies indicate that such nonlinear states play an important role in describing the transitional and turbulent flow regimes. First, their onset at a certain value of the Reynolds number enriches the state space, indicating an increased flow complexity. Searching for traveling waves at low Reynolds number one can seek the lower limit for the existence of alternative flow states, allowing to establish the *global stability threshold* of a flow (namely, the value of the Reynolds number below which the laminar solution remains unconditionally stable; see Ref. [31]). Moreover, traveling waves offer flashes of states visited by the chaotic flow, as observed in several experiments [20,32], showing good comparison to numerically computed traveling waves [11,12]. The experimental study in Ref. [33] found two unstable traveling waves in decaying pipe turbulence. The numerical study in Ref. [34] showed that known traveling waves in pipe flow are situated in a less energetic region between the laminar and turbulent flow, hence demonstrating their importance for the transition process rather than for sustaining the fully developed turbulent flow. Furthermore, heteroclinic connections between equilibria and traveling waves provide glimpses of the dynamics of trajectories wandering in the chaotic saddle [35,36]. All these studies suggest that traveling waves may be suitable for describing the main features of transitional and/or turbulent flows, as deeply discussed in Ref. [37] for flows such as plane Couette, plane Poiseuille, the pipe, and the square duct flow.

Another typical flow for which invariant solutions have been recently identified is the asymptotic suction boundary layer (ASBL), namely, the flow established on a flat plate when a constant homogeneous suction is applied at the solid wall. This flow has been often used as a model flow for studying transition to turbulence in boundary-layer flows, since it provides a parallel counterpart of the classical self-similar Blasius boundary-layer (BBL) solution. It is also relevant for flow control since the applied wall suction is known to increase considerably the linear stability threshold of a boundary-layer flow (although this might not be true for nonlinear stability). As discussed above, traveling waves are believed to make part of a hierarchy of nonlinear solutions being relevant to the turbulent transition. Therefore, investigating whether wall suction is indeed able to suppress these waves may give important clues for preventing the occurrence of transition to turbulence.

In recent studies, various two- and three-dimensional (2D and 3D) traveling waves have been computed for the ASBL flow [38–41]. These works have shown that, when walls having zero or very low permeability are considered, 2D invariant solutions nonlocalized in space exist from $\mathrm{Re} \approx 3000$, whereas localized 3D solutions can be found already at Re around 400 (the Reynolds number Re being based on the displacement thickness). Moreover, it is known that the ASBL can delay by far the growth of linear normal-mode disturbances compared to the BBL flow, the linear stability limit being $\mathrm{Re}_c \approx 54\,400$ for the ASBL [42–44], whereas the laminar BBL is unstable to small amplitude perturbations from $\mathrm{Re}_c \approx 520$ [44,45]. For small wall permeabilities, Refs. [39] and [46] have confirmed that wall suction has a stabilizing effect on low-amplitude perturbations. Nevertheless, in Ref. [39] it has been shown that finite-amplitude exact coherent solutions exist at lower values of the Reynolds number with respect to the Blasius flow where no suction is applied, provided that the permeability of the porous wall is sufficiently large. However, this study was limited to a 2D configuration, where transition to turbulence cannot be properly investigated. In a 3D configuration, for $\mathrm{Re} = 400$ and 500, edge states [26,27] and minimal energy perturbations on the edge of chaos [47] have been computed for vanishing wall porosity. Roughly in the same Reynolds number range there exist edge states also for the case of the BBL, as computed in Refs. [23,24]. Moreover, recent studies show that sustained turbulence is observed in ASBL flows at much lower Reynolds numbers. In fact, although earlier works [48] provided a critical Reynolds number for turbulence sustainment equal to $\mathrm{Re}_g = 367$, this threshold has been lowered to $\mathrm{Re}_g = 280$–333 [49], and very recently to $\mathrm{Re}_g \approx 270$ [50,51]. However, no previous study to the best of our knowledge has investigated the distance between this threshold value of Re for sustained turbulence and that at which a saddle-node (SN) bifurcation of exact coherent states arises, as it has been previously done for other flows [20,32]. Moreover, these previously mentioned studies are all limited to the case of zero wall-normal perturbation at the plate, which cannot be realistically achieved for a finite permeability of the wall. Computing 3D traveling waves for the ASBL flow at different values of the wall permeability and for low values of the Reynolds number, this work aims at identifying the threshold value of the Reynolds number for the existence of invariant solutions, as well as the influence of the wall permeability on this threshold. We show that a SN bifurcation arises already at $\mathrm{Re} = 225$, giving birth to two branches of traveling waves capable of leading the flow to turbulence, at least in a small domain.

The paper is organized in the following way: In Sec. II the flow configuration and the governing equations are presented. Section III presents the results: in particular, in Sec. III A invariant solutions in the shape of traveling waves are shown and discussed, whereas, Sec. III B provides the results of linearized and nonlinear direct numerical simulations to study the 3D instability of the traveling waves and the nonlinear evolution of the Navier-Stokes equations starting from them. Finally, conclusions can be found in Sec. IV.

II. DEFINITIONS

A. Governing equations

In this work, the search for 3D finite amplitude solutions in the asymptotic suction boundary layer flow over a flat plate is carried out, extending the 2D studies in Refs. [39,40]. The configuration is of infinite length in the streamwise $\check{x}$ direction and the spanwise $\check{z}$ direction. The truncated computational outer edge is situated at $\check{y} = \check{y}_\infty$. For free-stream parameters we will use subscript ∞, whereas variables without the $\check{}$ symbol refer to nondimensional quantities. The unit vectors are $\mathbf{i}$, $\mathbf{j}$ and $\mathbf{k}$, the velocity field is composed by the streamwise, wall-normal, and spanwise components, i.e., $\check{\mathbf{u}} = \check{u}\mathbf{i} + \check{v}\mathbf{j} + \check{w}\mathbf{k}$, whereas $\check{p}$ is the pressure and time is $\check{t}$.

At the plate, having wall-normal coordinate $\check{y} = 0$, a constant uniform suction $\check{V} = -\check{V}_0$ ($\check{V}_0 > 0$) is applied with the aid of a porous wall, usually for the purpose of stabilizing the flow. As sketched in Fig. 1, applying a constant uniform suction $\check{V} = -\check{V}_0$ ($\check{V}_0 > 0$) to a boundary-layer flow, the flow changes gradually from the well-known Blasius solution near the leading edge to an asymptotic

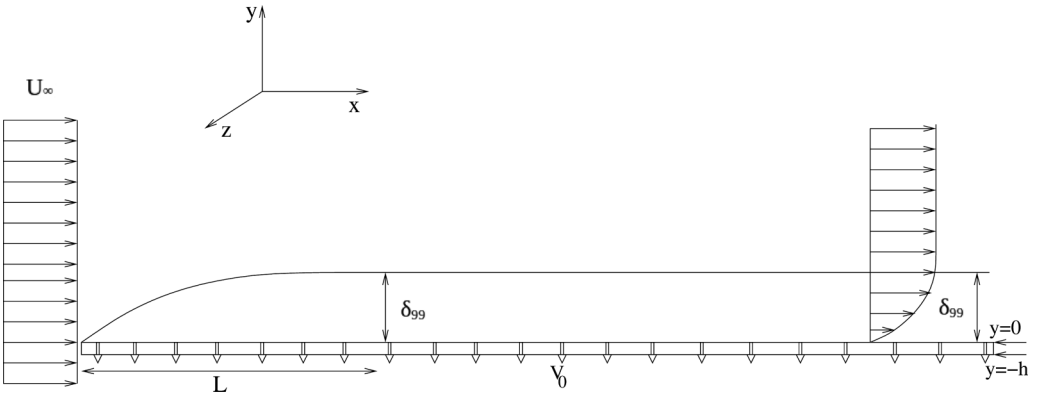

FIG. 1. The laminar flow in the asymptotic suction boundary layer with constant wall suction $\check{V} = -\check{V}_0$ ($\check{V}_0 > 0$). The boundary layer thickness is denoted by $\check{\delta}_{99}$, and $\check{L}$ is the distance from the leading edge starting from which the laminar flow is dependent uniquely on $\check{y}$. The wall suction is applied at $\check{y} = -\check{h}$, where the pressure and wall normal velocity perturbations are zero, whereas, at $\check{y} = 0$, the pressure and wall normal velocity perturbations are computed using the Darcy's law. The $\check{}$ symbols placed on top of the dimensional flow variables are omitted for brevity.

form at a distance L in the streamwise direction where the laminar flow becomes independent of $\check{x}$ and strictly parallel. This asymptotic flow solution is called the asymptotic suction boundary layer (ASBL). The distance L is governed by the formula $(-\check{V}_0/\check{U}_\infty)^2\check{U}_\infty\check{x}\check{\nu}^{-1} = 4$ according to Ref. [52], where $\check{\nu} = \check{\mu}/\check{\rho}$ is the kinematic viscosity, $\check{\mu}$ the dynamic viscosity, $\check{\rho}$ the density of the fluid and $\check{U}_\infty$ the streamwise free-stream speed. At $\check{y} = 0$ we have $(\check{U}, \check{V}) = (0, -\check{V}_0)$ and $\check{U} = \check{U}_\infty$ as $\check{y} \to \infty$. Sufficiently far from the leading edge (as $\check{x} \to \infty$) one obtains an exact asymptotic solution by setting $\partial\check{U}/\partial\check{x} = 0$, yielding the following flow features: $\check{U} = \check{U}(\check{y})$, constant wall normal velocity in the whole domain ($\check{V} = -\check{V}_0$), and zero pressure gradient $\check{\boldsymbol{\nabla}}\check{P}$. Injecting these conditions into the incompressible Navier-Stokes equations together with the continuity condition

$$\check{\boldsymbol{u}}_{\check{t}} + \check{\boldsymbol{u}} \cdot \check{\boldsymbol{\nabla}}\check{\boldsymbol{u}} + \frac{1}{\check{\rho}}\check{\boldsymbol{\nabla}}\check{p} - \check{\nu}\check{\boldsymbol{\nabla}}^2\check{\boldsymbol{u}} = \boldsymbol{0}, \quad \check{\boldsymbol{\nabla}} \cdot \check{\boldsymbol{u}} = 0, \tag{1}$$

the exact (dimensional) asymptotic solution $\check{U}(\check{y}) = \check{U}_\infty[1 - \exp(-\check{V}_0\check{y}/\check{\nu})]$, $\check{V} = -\check{V}_0 = \text{const}$, is obtained. Before nondimensionalizing the system of equations we consider the conditions at the plate. The difference from the BBL configuration is the suction condition at the plate for the normal velocity $\check{v}$. We assume $\check{u} = \check{w} = 0$ at $\check{y} = 0$. To define the conditions of $\check{v}$ at the plate, of thickness $\check{h}$, we use the Darcy's law, which can be derived by considering Stokes flow in the cavity of the porous media and averaging over the pore volume. The Darcy's law gives a linear relation between the average fluid velocity and the pressure difference or $\check{v} = -(\check{K}/\check{\mu})\check{\boldsymbol{\nabla}}\check{p}$, where $\check{K}$ is the permeability of the medium. To find nonlinear solutions the laminar flow is perturbed, hence at the boundary $\check{y} = 0$ we consider the base flow $(-\check{V}_0, \check{P}_1)$ plus a perturbation $(\check{v}', \check{p}')$ and perturbation-free conditions at $\check{y} = -\check{h}$, $(-\check{V}, \check{P}) = (-\check{V}_0, \check{P}_0)$ (see the conditions at the porous flat plate in Fig. 1). Using these conditions we recover the following dimensional equality:

$$\check{v}' = -\frac{\check{K}}{\check{h}\check{\mu}}\check{p}'. \tag{2}$$

Equation (2) provides the relation between the pressure and the wall-normal velocity perturbation at $\check{y} = 0$ [53]. This simple model is usually considered to be valid for steady and linear porous-media flows, whereas, for nonlinear flows, a quadratic velocity term [54] has to be added in the momentum balance, resulting in the Forchheimer equation. However, in Ref. [40] it has been demonstrated that this quadratic interaction term has negligible influence on the flow stability when low permeabilities

such as those considered in the present work are considered. Moreover, for unsteady flows, a time delay term can be also added to the momentum balance [55], which for small values of the Reynolds number is quadratic with respect to the velocity [56]. Although this term is of considerable amplitude when instantaneous velocities are considered, it can be straightforwardly neglected when modeling the dynamics of perturbations, which are many orders of magnitude smaller than the reference velocity.

The governing equations are now nondimensionalized using the unidirectional free-stream speed $\check{U}_\infty$, the density $\check{\rho}$, and the displacement thickness $\check{\delta}_*$:

$$\mathbf{u} = \frac{\check{\mathbf{u}}}{\check{U}_\infty}, \quad \mathbf{x} = \frac{\check{\mathbf{x}}}{\check{\delta}_*}, \quad p = \frac{\check{p}}{\check{\rho}\check{U}_\infty^2}, \quad t = \frac{\check{t}\check{U}_\infty}{\check{\delta}_*}, \tag{3}$$

with the displacement thickness defined as $\check{\delta}_* = \int_0^{\check{y}_\infty}(1 - \check{U}(\check{y})/\check{U}_\infty)d\check{y}$. Integration reveals that $\check{\delta}_* = \check{\nu}/\check{V}_0$, using the expression of $\check{U}(\check{y})$ given above. The nondimensionalized Navier-Stokes equations and the continuity equation are

$$\boldsymbol{u}_t + \boldsymbol{u}\cdot\boldsymbol{\nabla}\boldsymbol{u} + \boldsymbol{\nabla}p - \frac{\check{\nu}}{\check{\delta}_*\check{U}_\infty}\nabla^2\boldsymbol{u} = \mathbf{0}, \quad \boldsymbol{\nabla}\cdot\boldsymbol{u} = 0, \tag{4}$$

where $\check{\delta}_*\check{U}_\infty/\check{\nu}$ is the Reynolds number Re and the components of the laminar base flow $\mathbf{U}$ are

$$U(y) = 1 - e^{-y}, \quad V = -\frac{1}{\mathrm{Re}}. \tag{5}$$

Using the fact that $\check{\delta}_* = \check{\nu}/\check{V}_0$ we find that $\mathrm{Re} = \check{U}_\infty/\check{V}_0$. To search for 3D solutions we impose a perturbation $\epsilon\boldsymbol{u}'$ (where ϵ is an unknown amplitude to be solved for) on the laminar base flow and substitute $\boldsymbol{u}$ in Eq. (4). Then, subtracting the pure laminar flow terms, one obtains the equations governing the perturbation:

$$\boldsymbol{u}'_t + \boldsymbol{\nabla}p' - \frac{1}{\mathrm{Re}}\nabla^2\boldsymbol{u}' + (\mathbf{U}\cdot\boldsymbol{\nabla})\boldsymbol{u}' + (\boldsymbol{u}'\cdot\boldsymbol{\nabla})\mathbf{U} + \epsilon\boldsymbol{u}'\cdot\boldsymbol{\nabla}\boldsymbol{u}' = \mathbf{0}, \tag{6}$$

$$\begin{aligned} &u' = w' = 0, \quad v' \neq 0 \quad \text{at} \quad y = 0, \\ &\boldsymbol{u}' \to 0 \quad \text{as} \quad y \to \infty, \end{aligned} \tag{7}$$

with periodic conditions in the spanwise and downstream direction, no-slip for u' and w' at the wall, whereas v' is linked to p' through Eq. (2) (the numerical implementation of this condition will be presented in detail in Secs. II B and II D). All velocity components decay exponentially with y as presented in the same section. Being the laminar flow components of Eq. (6) constants or functions of y only, allows us to express the perturbation $\boldsymbol{u}'$ as a Fourier series having streamwise wave number α, spanwise wave number β, and an eigenvalue in general defined as $c \in \mathbb{C}$. The eigenvalue represents the phase speed and growth rate of the perturbation generally expressed as $\boldsymbol{u}' = \sum_{b,j}\boldsymbol{u}^{(bj)}(y)\exp[Ib\alpha(x - ct)]\exp(Ij\beta z)$, where $I = +\sqrt{-1}$, $b = -NX,...,+NX$ and $j = -NZ,...,+NZ$ are the streamwise and spanwise Fourier indices, and $\boldsymbol{u}^{(bj)}(y)$ is expressed in a classical Chebyshev series with $NY + 1$ polynomials T_i and has no symmetry imposed in y. We consider temporal growth of the perturbation, hence the streamwise and the spanwise wave numbers $\alpha, \beta \in \mathrm{Re}$ and $c \in \mathbb{C}$ in general. However, since the traveling wave (TW) sought for should propagate at a constant real speed maintaining the same amplitude over time, we impose $c_i = \Im(c) = 0$ and we seek for $c_r = \Re(c)$, which represents an unknown. The phase of the solution is fixed by imposing the following normalization condition on one of the Fourier modes:

$$v'^{(b=1,j=-1)}(y = 3) = 1. \tag{8}$$

The real flow domain in y $[0, \infty)$ is truncated to the computational domain $[0, y_\infty]$ and transformed to the interval $[-1, +1]$ in γ through the mapping $y = a(1 + \gamma)/(b - \gamma)$, where $a = y_i y_\infty/(y_\infty - 2y_i)$, $b = 1 + 2a/y_\infty$ and y_i is the distance from the plate where half of the

collocation points are situated. We use the well-known Gauss-Lobatto distribution for defining the collocation points $\gamma_k = \cos(k\pi/NY)$, for $k = 0, 1, 2, \ldots, NY$. A time-independent problem is solved by viewing the flow in a frame of reference $x - c_r t \to X$ moving with the wave speed c_r, thus $\partial_t \to -c_r \partial_X$.

B. Boundary conditions

At $y = 0$ we assume $u' = w' = 0$, whereas for the v' component a boundary condition taking into account the permeability of the porous plate has to be considered. To derive the v' boundary conditions at $y = 0$ we carry out the operation $\partial_x(\mathbf{i} \cdot (6)) + \partial_z(\mathbf{k} \cdot (6))$. Then applying the continuity equation and substituting the pressure using the nondimensional form of the Darcy's law [Eq. (2)] yields the following boundary condition:

$$v'_{yyy} + v'_{yy} - \frac{\mathrm{Re}}{a}(v'_{xx} + v'_{zz}) + \mathrm{Re}v'_x + \epsilon\mathrm{Re}(v'_x u'_y + v'_z w'_y - v' v'_{yy}) = 0, \quad a = \frac{\check{U}_\infty \check{K}}{\check{\nu}\check{h}}, \tag{9}$$

where a is the nondimensional permeability.

In the free stream, truncated at $y = y_\infty$, we impose decaying perturbations where the Fourier amplitudes obey the condition

$$\frac{d\boldsymbol{u}^{(bj)}(y)}{dy} + q\boldsymbol{u}^{(bj)}(y) = \mathbf{0}, \quad q = \frac{1}{2}(1 + \sqrt{1 + 4k^2}), \tag{10}$$

where $k^2 = \alpha^2 b^2 + \beta^2 j^2$ and $\boldsymbol{u}^{(bj)}(y)$ is the y-dependent function in the Fourier series previously provided. These boundary conditions can be derived from the Navier-Stokes equations and show exponential decay with y on all Fourier modes. The asymptotic conditions (10) are obtained linearizing the perturbation Eq. (6) and assuming constant laminar flow. Neglecting the effects of viscosity the equations leading to decaying perturbations in the free stream are recovered. Both boundary conditions introduced above are incorporated in the vector F representing the governing equations [see Eq. (A5) in the Appendix].

C. Traveling wave computation

We look for TW solutions of the governing equation (6) with the above boundary conditions, respecting the reflect symmetry defined as

$$\boldsymbol{Z} : (u, v, w, p)(x, y, z, t) = (u, v, -w, p)(x, y, -z, t). \tag{11}$$

In Refs. [26,41] TWs and periodic orbits respecting a shift-and-reflect symmetry have been found for $\mathrm{Re} > 300$. However, since one of the main aims of this work is to ascertain whether the value of Re for which turbulence is sustained may be linked to a SN bifurcation of exact coherent states, we choose to focus on a different flow symmetry for trying to lower to $\mathrm{Re} \leqslant \mathrm{Re}_g$ the value of Re for which any TW can be found. The TW sought for can be expressed using the following Fourier series:

$$\begin{bmatrix} u' \\ v' \\ w' \\ p' \end{bmatrix} = \sum_{b=0}^{NX} \sum_{j=0}^{NZ} \sum_{i=0}^{NY} \begin{bmatrix} \hat{u}_{bji} T_i[\gamma(y)] \cos j\beta z \\ \hat{v}_{bji} T_i[\gamma(y)] \cos j\beta z \\ \hat{w}_{bji} T_i[\gamma(y)] \sin j\beta z \\ \hat{p}_{bji} T_i[\gamma(y)] \cos j\beta z \end{bmatrix} e^{Ib\alpha(x-ct)} + \mathrm{c.c.}, \tag{12}$$

where c.c. is the complex conjugate and $\hat{\boldsymbol{u}}_{bji}$ are the unknown Fourier coefficients to be solved for. To measure the wave amplitude we construct the parameter Amp_{3D} using the coefficients of the first

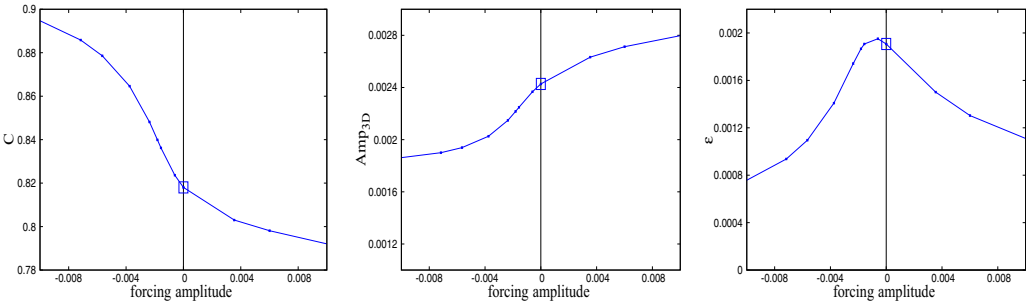

FIG. 2. The search for the point where $f_A = 0$ with $\mathrm{Re} = 600$, $\alpha = 0.30$, $\beta = 1$, and $a = 0$ using a low numerical resolution. A trace-out is shown of the phase speed c, of the amplitude Amp_{3D}, and ϵ vs f_A. The relevant solution at $f_A = 0$ is pointed out by the open square and can be used to map out solutions in parameter space, e.g., to finite permeabilities $a \neq 0$. A more exhaustive proof of convergence of the unforced solutions is shown later.

Fourier mode [namely, $\hat{\boldsymbol{u}}_{bji}$ with $(b, j) = (1, 1)$]:

$$\mathrm{Amp}_{3D} = \sqrt{\epsilon^2 \sum_{i=0}^{NY} |\hat{u}_{11i}|^2 + |\hat{v}_{11i}|^2 + |\hat{w}_{11i}|^2}, \tag{13}$$

ϵ being the amplitude of the TW. To narrow down the dimensions of the parameter space (α, β, Re and a) the study is limited to $a = 0$, 3.85×10^{-4} and 0.01. The case $a = 3.85 \times 10^{-4}$ being used in the experiments of Ref. [44], we use the same parameter settings as those used therein, where $\hat{U}_\infty = 5\,\mathrm{ms}^{-1}$, $\hat{\nu} = 1.5 \times 10^{-5}\,\mathrm{m}^2\,\mathrm{s}^{-1}$, and $\hat{h} = 3.2\,\mathrm{mm}$. The computations are restricted to low permeabilities a in order to justify the use of the Darcy permeability model. In fact, in Ref. [40] considerable differences have been found between 2D Tollmien-Schlicting waves computed using the Darcy and the Forchheimer wall models (with the latter being the more physically correct), when values of the wall permeability $a > 0.7$ were used. When studying the linear stability of these 2D TWs, some differences were observed even at lower a, around 0.20. Whereas, negligible differences between the results obtained using the two permeability models have been found for the values of a considered here.

Concerning the Reynolds number, it is known that the critical point for linear instability is found at very large Reynolds number ($\mathrm{Re}_c \approx 54\,400$ [42,44,57]), whereas sustained turbulence is observed for $\mathrm{Re} > 270$ [50,51]. In order to search for nonlinear solutions one can impose a 3D perturbation on the Tollmien-Schlicting (TS) waves computed in Ref. [39] and look for a neutrally stable point from where the 3D solutions can bifurcate. To avoid a time-consuming search of nonlinear solutions at low Re, either starting from $\mathrm{Re} = 54\,400$ or bifurcating from a TS-wave, a forcing function $f(y, z)$ is added to the Navier-Stokes equations. The purpose is to find a bifurcation point at low Re, bringing the forcing to zero for a $\boldsymbol{u}'$ having finite amplitude. The definition of f, along with further details on the procedure used for finding the TWs, are provided in the Appendix. In order to find relevant 3D nonlinear solutions, the point of vanishing amplitude f_A of the forcing function f [see Eq. (A1) and discussion below] needs to be located, as shown in Fig. 2. The relevant solutions represented by the open square symbols in the three subframes of Fig. 2 will be used as initial guess allowing the computation of TWs in parameter space.

The code used for solving the problem with the boundary conditions discussed in Sec. II B is a slightly modified version of the one used for producing nonlinear TW solutions of the BBL flow [18]. For the purpose of validation the nonlinear 2D results contained in Refs. [58,59] were reproduced. Then, the code has been modified to tackle the case of the asymptotic suction boundary layer flow adding the wall-suction terms. For this case the linear stability of the laminar

ASBL has been computed, reproducing the critical Reynolds number $\mathrm{Re}_c \approx 54\,400$ according to Refs. [42–44,57] imposing a zero perturbation condition also on the wall-normal component of the velocity. It is worth to point out that this critical Reynolds number decreases considerably when using a small but finite permeability [39].

D. Direct numerical simulations

Once the nonlinear TWs have been computed for different permeabilities, wave numbers and Reynolds numbers, the linear and nonlinear stability of some selected solutions have been analyzed using linearized or fully nonlinear direct numerical simulations (DNS). Since a TW pertaining to a subspace with given symmetry can be prone to instability having a different symmetry, no symmetry has been imposed in the DNS. For allowing the developing of subharmonic modes, we choose a computational box with dimensions $L_x \times L_y \times L_z = 4\pi/\alpha \times y_\infty \times 4\pi/\beta$. On this computational domain, the Navier-Stokes equations, written in perturbative formulation, are discretized and solved using a finite-difference fractional-step method with second-order accuracy in space and time [60]. The number of grid points has been chosen after careful validation with respect to previous results [39], as well as by comparing the results with those of simulations performed doubling and halving the grid points in each direction. Concerning the boundary conditions, at the wall the nondimensional Darcy's law for the wall-normal perturbations given in Eq. (2) is imposed, whereas a zero perturbation condition is used for the streamwise and spanwise velocities; at the upper boundary, all perturbations are set to zero, whereas in the spanwise and streamwise direction periodicity is imposed for the three velocity components. For ensuring that the incompressibility constraint holds on the wall boundary, the velocity and pressure should be ideally solved for simultaneously. In this work, for determining the wall velocity at the prediction step of the fractional step method we have used the pressure value obtained at the previous time step, that we have opportunely modified in the correction step for respecting the incompressibility constraint. In this way, we ensure a divergence as small as 10^{-15} for time step values $dt < 0.5$. The Navier-Stokes equations in the perturbative form (6) have been used for both the linear and nonlinear simulations, $\mathbf{U}$ indicating now the TW solution. The linear simulations have been initialized by superposing to the base flow the TW solution; the perturbation of this relative fixed point, denoted as $\mathbf{u}''$, has been initialized by a random zero-mean noise of small amplitude 10^{-10} for the spanwise velocity components, multiplied by an envelope function centered at $y = 3$. The linear time evolution of the perturbations has then been studied, by neglecting the perturbative nonlinear terms in Eqs. (6). The most unstable mode recovered by linearized DNS is then used for initializing the nonlinear simulations. Different initial energies, E_0, have been used for scaling the recovered mode, which is then superposed to the TW solution. The long-time evolution of this perturbation of the TW has then been tracked in order to ascertain whether it might succeed at inducing transition to turbulence.

III. RESULTS

The main objective of the present study is to find TW solutions of the governing Eqs. (6) for low values of the Reynolds number. We will also study the linear stability of the recovered TWs in order to get insight into their role in state space. To further the understanding of the considered TWs, direct numerical simulations of the Navier-Stokes equations will be also carried out to investigate whether the flow turns laminar or turbulent, starting from the neighbourhood of some selected TWs.

A. The TW solutions

For the three chosen values of the nondimensional permeability ($a = 0$, 3.85×10^{-4} and 0.01) and given wave numbers α and β, we search for the minimum Reynolds number at which 3D TW solutions having the chosen symmetry arise in a SN bifurcation, namely, $\mathrm{Re}_{SN}(a)$. Using the nonforced solution in Fig. 2 as an initial guess (open square symbol) we map out TWs in parameter space, with the intention of seeking their existence at different (possibly lower) values of Re. The

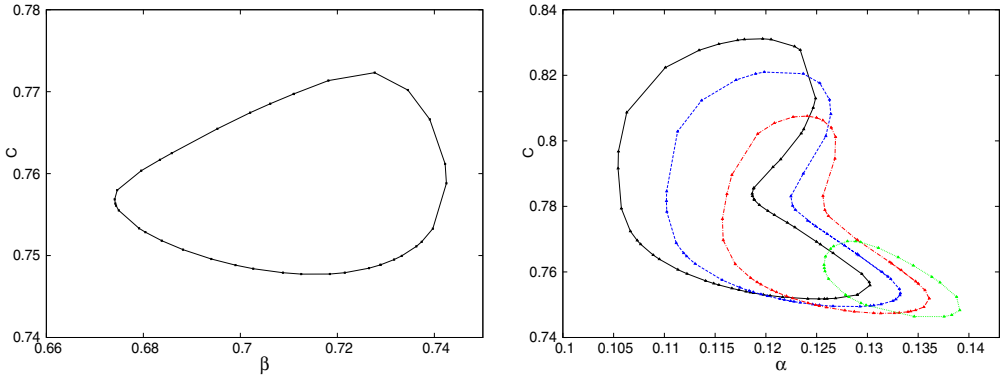

FIG. 3. Left: the wave speed c as a function of β for $(\mathrm{Re}, \alpha, a) = (231, 0.129, 0)$ using a truncation of $(NX, NY, NZ) = (8, 100, 7)$. This curve is used as a point of departure for mapping out the TW in α on the right. Right: the solutions mapped out in α using equally spaced values of β from the left figure: $\beta = 0.68$ (solid black line), $\beta = 0.695$ (blue dashed), $\beta = 0.711$ (red dash-dotted), and $\beta = 0.736$ (green dotted).

following computations are repeated a number of times: one first moves in Re until a saddle node is found (i.e., the point where the solutions bend back toward higher Re), for a fixed value of α and β. Then, families of solutions are traced out in β using a Re close to the saddle node. In the next step, for several equally spaced values of β chosen from the above mentioned curve, α is varied, as shown in Fig. 3 providing the wave speed of the obtained solutions as well as in Fig. 4 providing the related amplitude measured by the maximum value of the spatial mean of the streamwise perturbation velocity. To avoid a lengthy process, due to the infinite amount of combinations of α and β, the search reaches its final phase when a family of solutions having a sufficiently small interval in both α and β is obtained. This procedure is shown in Fig. 3 for $a = 0$ and $\mathrm{Re} = 231$ showing fairly narrow intervals in both wave numbers ($0.67 \leqslant \beta \leqslant 0.74$ and $0.105 \leqslant \alpha \leqslant 0.14$).

To make the computations feasible we select those values of α corresponding to solutions situated near the middle of each family of solutions in Figs. 3 and 4 (right plots). This gives us four combinations of (α, β), which are used for searching for the minimum Reynolds number $\mathrm{Re}_{SN}(a)$. Figure 5 shows wave speed (left plot) and amplitude (right plot) of the continuation curves of the solutions obtained for $a = 0$ and different values of α and β leading to the determination of $\mathrm{Re}_{SN}(a)$. The inset in the left plot of Fig. 5 shows a proof of convergence with respect to NX, NY

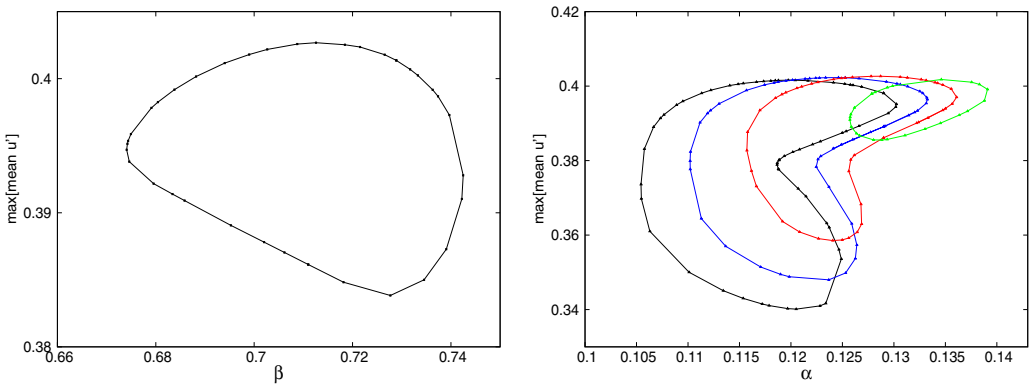

FIG. 4. Same as in Fig. 3 for the maximum value of the spatial mean of the streamwise perturbation velocity. See Fig. 3 for details of each curve.

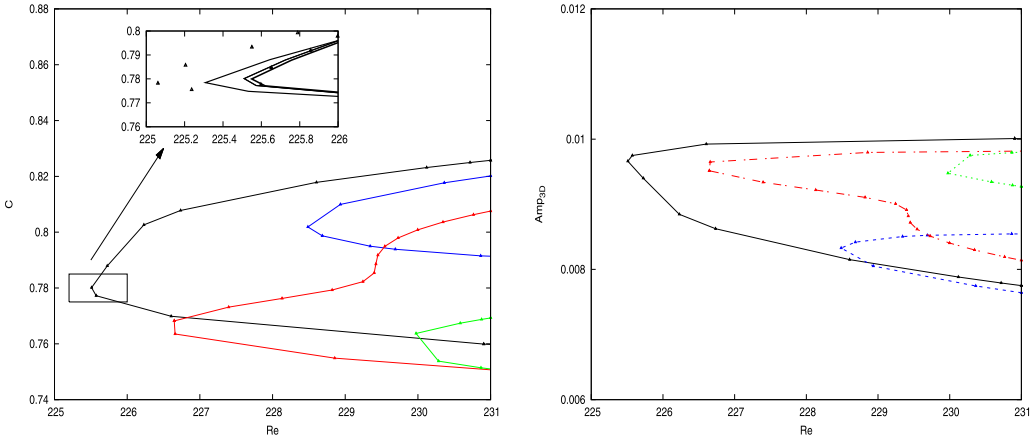

FIG. 5. The search of Re_{SN} for $a = 0$ for a combinations of α and β selected from Fig. 3, using a default truncation of $(NX, NY, NZ) = (8, 100, 7)$. The curves show wave speed (left) and amplitude (right) for $(\alpha, \beta) = (0.112, 0.680)$, black solid line, (0.124,0.695) blue dashed line, (0.124,0.711) red dashed-dotted line, and (0.129,0.736), green dotted line. For $(\alpha, \beta) = (0.112, 0.680)$ we reach $\mathrm{Re} \approx 225$, which is thus defined as $\mathrm{Re}_{SN}(a = 0)$. The inset in the left plot shows a proof of convergence with respect to NX, NY and NZ using the truncations $(NX, NY, NZ) = (8, 100, 7)$ solid line, (8,100,11) dashed, (8,120,7) dashed-dotted, and (12,100,7) triangles.

and NZ, using the truncations $(NX, NY, NZ) = (8, 100, 7)$ solid line, (8,100,11) dashed, (8,120,7) dashed-dotted and (12,100,7) triangles. The continuation branch found with (8,100,7) overlaps that obtained with (8,120,7), whereas a very small difference is recovered when comparing the default truncation with (8,100,11) and (12,100,7). Further convergence analyses with respect to the number of modes are shown in Fig. 6 (see caption) for the case with $a = 0.01$, providing a satisfying agreement. The same figure provides a convergence study with respect to the wall-normal domain length y_∞, which should be sufficiently high to ensure an exponential decay of the perturbations at the upper boundary. For $a = 0$, solutions obtained using $y_\infty = 40$ (open red squares) are compared with the default value of $y_\infty = 25$ (solid red line), providing a good agreement.

Both Figs. 5 and 6 show that for $(\alpha, \beta) = (0.112, 0.680)$ and $a = 0$, a TW solution is obtained at a value of $\mathrm{Re} \approx 225$, which constitutes our best estimate of the value of $\mathrm{Re}_{SN}(a = 0)$; this is below the value of observed sustained turbulence which has been found by several authors to be around 300 (more precisely, $\mathrm{Re}_g \approx 270$ according to Refs. [50,51], whereas $\mathrm{Re}_g = 367$ was reported in a less recent work [48]). No lower values of $\mathrm{Re}_{SN}(a = 0)$ have been provided in the literature to the best of the authors knowledge, therefore one can consider the estimated value of $\mathrm{Re}_{SN}(a = 0) \approx 225$ as a dividing point in state space. For $\mathrm{Re} < \mathrm{Re}_{SN}$, the laminar flow might be a global attractor, at least in the subspace with reflect symmetry defined in Eq. (11); for $\mathrm{Re} \geqslant \mathrm{Re}_{SN}$, alternative finite amplitude solutions cohabit the state space with the laminar attractor. The same procedure is carried out for the remaining two values of a. The curves used for defining $\mathrm{Re}_{SN}(a)$ are shown in Fig. 6 and summarized in Table I (also providing a comparison with the ASBL 2D case studied in Ref. [39] and the BBL in Ref. [18]). The values of the boundary layer thickness, δ_{99}, of the base flow plus three TWs with different wall porosity versus Re have been also plotted in Fig. 7. For all the values of a considered here, the TWs induce a consistent departure of the boundary layer thickness from the value associated to the ASBL laminar solution, $\delta_{99} = 4.605$. Values as high as $\delta_{99} \approx 19$ are reached for the upper branch states at the largest considered Reynolds numbers. The wall porosity appears to have an influence on the boundary layer thickness, especially on the lower branch states for high values of the Reynolds numbers, whose δ_{99} increases with Re for $a = 0.01$, whereas it decreases for $a = 0$. A critical aspect of all 3D family of solutions is the difficulty to resolve well the upper

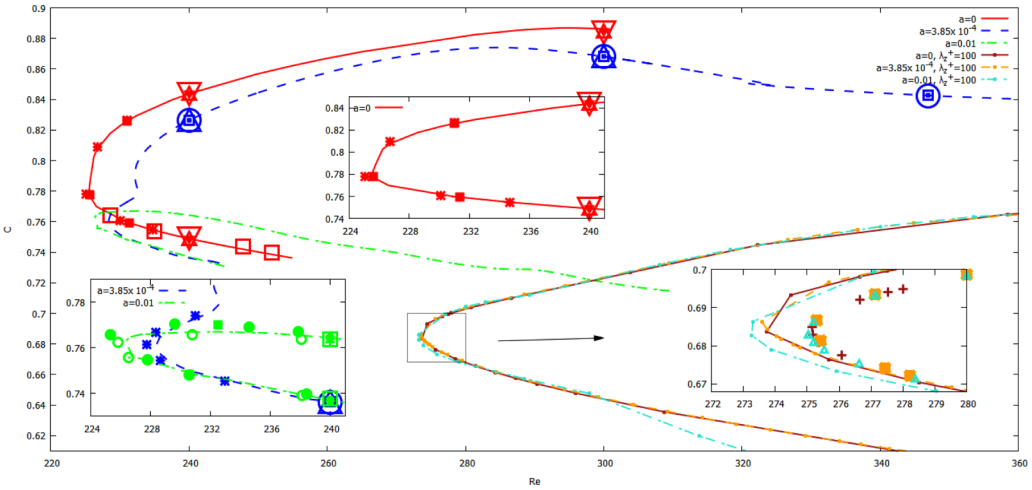

FIG. 6. The wave speed c of the TWs mapped out in Re for the plate porosity $a = 0$, 3.85×10^{-4} and 0.01 for the values of $\alpha = \alpha_{SN}$ and $\beta = \beta_{SN}$ providing the minimum Reynolds number Re_{SN}; see Table I. The point where the curves bend back is the node point that defines Re_{SN}. The curves are shown as far as convergence can be confirmed, and the symbols correspond to the convergence runs. For $a = 0$ (red) and 3.85×10^{-4} (blue) the default truncation is $(NX, NY, NZ) = (8, 100, 7)$, and proof of convergence is shown using (8,100,9), (8,100,11), (8,120,7), (10,100,7), and (12,100,7). For $a = 0.01$ (green) a default truncation $(NX, NY, NZ) = (8, 115, 7)$ is used, and for the convergence runs (8,115,9), (8,115,11), (8,135,7), (10,115,7), (11,115,7), (7,115,7), and (7,115,11). In order to prove convergence in NX and NZ for $a = 0.01$ the truncation (7,115,7) should be compared with (11,115,7) and (7,115,11). For all values of a a perfect match is seen comparing the various truncations. For $a = 0$, solutions using $y_\infty = 40$ (open red squares) are compared with the default value of 25 (solid red line), giving a good agreement. The case with $\mathrm{Re} = 347$ and $a = 3.85 \times 10^{-4}$ is the flow case experimentally studied in Ref. [44]. The TW solutions with $\lambda_z^+ = 100$ are shown at the very bottom of the figure for $a = 0$ (brown), $a = 3.85 \times 10^{-4}$ (orange), and $a = 0.01$ (turquoise). The dotted lines correspond to a truncation of (6,100,5) and match well the higher resolution case with (8,120,7).

branch, i.e., the branch representing TW of larger amplitude and lower values of c. This is shown in Fig. 6 where convergence could be proven only for the initial part of the upper branches (lower part of the curves on the Re-c plane).

From Fig. 6 and Table I (first three lines) one can observe that, even if the values of Re_{SN} depend slightly on the wall permeability a, the shape of the solution branches changes dramatically with a once departing from Re_{SN}. However, one can recall that the reported bifurcation curves are related to different values of the spanwise wave number β, whereas it is known that turbulent flows have a given dominating mean spanwise spacing $\lambda_z^+ = \check{\lambda}_z \check{u}_\tau / \check{\nu} \approx 100$ [61], where $\check{u}_\tau$ is the friction velocity $\check{u}_\tau = \sqrt{\frac{\check{\tau}_w}{\check{\rho}}}$, $\check{\tau}_w$ referring to the shear stress at the wall. Expressing λ_z^+ using the total mean velocity $u_m(y)$ we get

$$\lambda_z^+ = \frac{2\pi}{\beta} \sqrt{\mathrm{Re} \frac{du_m}{dy}\bigg|_{y=0}}, \tag{14}$$

where $u_m = U(y) + \epsilon \tilde{u}^{(0,0)}(y)$ is the solely y-dependent part of the total flow, i.e., the laminar flow plus that part of the perturbation being dependent on y only. We have thus computed TW solutions having a spanwise wavelength λ_z^+ fixed to the turbulent value of 100, which are obtained for the set of parameters reported in the middle of Table I. This strongly changes the bifurcation diagram in Fig. 6: the curves near the node now overlap for all permeabilities a studied and, compared to the case where λ_z^+ can change freely, Re_{SN} increases to 275; see Table I for further details. From

TABLE I. The table shows the minimal Re overall (= Re_{SN}) of the 3D flow states (3D) for the values of a studied (from first to third line). Keeping λ_z^+ fixed to 100 increases the value of both α and β remarkably and sets the Re_{SN} back to 275 (fourth to sixth lines). The Re_{SN} of the 2D flow for the same three values of a are shown in the next three lines for the purpose of comparison [39]. The last row displays the same values for the Blasius flow [18] and shows no resemblances when comparing with the ASBL. The value of y_∞ used for each of these solutions is reported too, Fig. 6 showing a proof of convergence with respect to these selected values.

a	α_{SN}	β_{SN}	Re_{SN}	c	λ_z^+	y_∞	Flow state
0	0.112	0.680	225	0.78	139	25	3D
3.85×10^{-4}	0.128	0.726	228	0.76	131	30	3D
0.01	0.129	0.707	226	0.76	134	30	3D
0	0.204	1.042	275	0.68	100	25	3D
3.85×10^{-4}	0.203	1.043	275	0.68	100	25	3D
0.01	0.204	1.042	275	0.68	100	25	3D
0	0.200		3168	0.40	N/A	N/A	2D
3.85×10^{-4}	0.205		3128	0.40	N/A	N/A	2D
0.01	0.168		2324	0.44	N/A	N/A	2D
	0.344	1.658	496	0.434	65	N/A	3D Blasius

these results it appears that changing the permeability affects the spanwise size (in wall units) of the coherent structures able to be sustained within the flow at different values of Re, allowing the sustainment of TWs of larger spanwise size at lower Reynolds numbers. Clearly, this effect is no longer visible when the spanwise size of the TW (in wall units) is imposed.

Moreover, looking at Table I, one can notice an appreciable difference in Re_{SN} between the 2D and the 3D waves. Re_{SN} is more than 10 times lower for the 3D states and the wave speed is almost twice than that of the 2D states. The large values of Re_{SN}^{2D} indicate the minor physical importance of 2D Tollmien-Schlicting waves to the turbulent transition which can be observed already at $\mathrm{Re}_g \approx 300$. The table shows no strong difference in $\mathrm{Re}_{SN}(a)$ for the 3D states, the combination (α, β) and the value of c being slightly different for the considered values of a. Looking at the bifurcation curves in Fig. 6 as a whole, one can notice that the differences in c are noticeable when moving away from the node. Moreover, the bifurcation curves for $a = 0$ and $a = 3.85 \times 10^{-4}$ are fairly close to

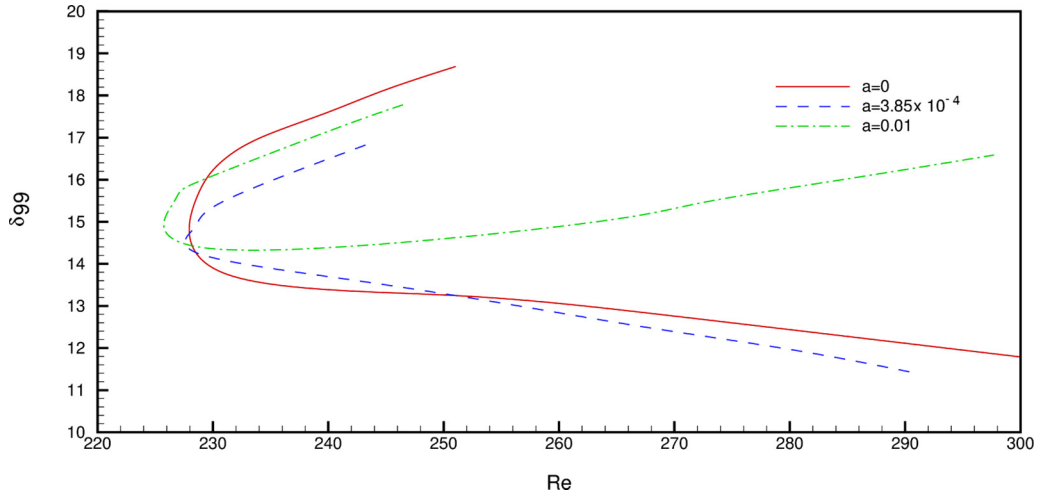

FIG. 7. The boundary layer thickness of the three TWs shown in red, blue, and green in Fig. 6 superposed to the ASBL base flow: $a = 0$ (red) $a = 3.85 \times 10^{-4}$ (blue), and $a = 0.01$ (green).

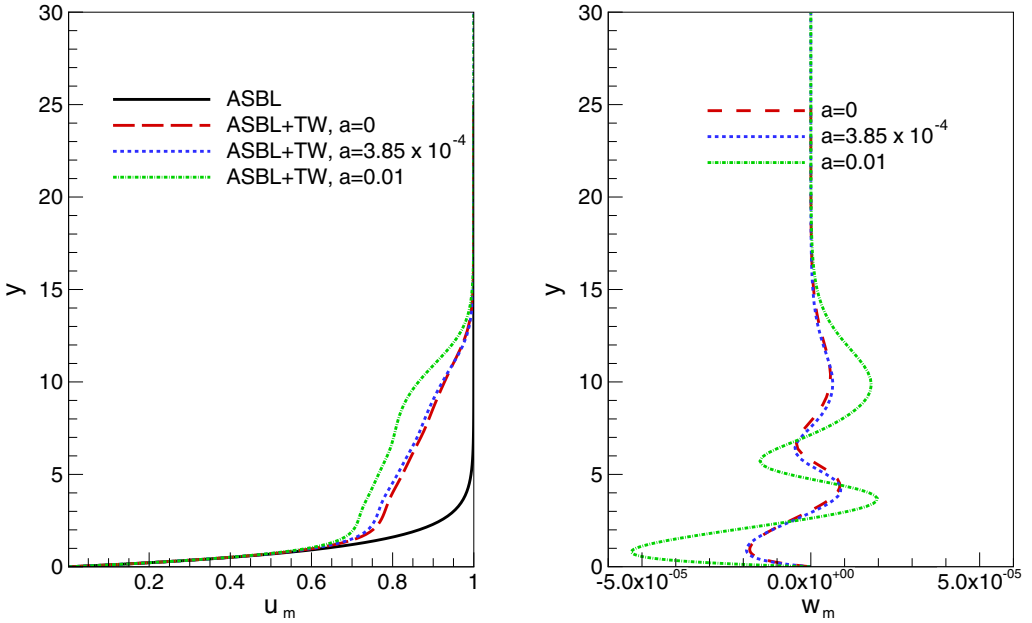

FIG. 8. Mean velocity profiles: streamwise (left plot) and spanwise (right plot) velocities, u_m and w_m, of the lower branch solutions near the node at $\mathrm{Re} = 240$ with wave numbers $\alpha = \alpha_{SN}$ and $\beta = \beta_{SN}$ for permeabilities $a = 0$ (red solid), 3.85×10^{-4} (blue dashed), and 0.01 (green dotted); see legend.

each other (see Fig. 6), whereas a dramatic difference is seen when comparing those for $a = 0$ and 0.01. Hence, it seems that, for sufficiently small values of the permeability, the extra terms in Eq. (9) are negligible and the use of a zero perturbation condition for v' might be acceptable. This has been discussed for the 2D case in Ref. [39] and appears to be confirmed also in this 3D study.

The streamwise and spanwise components of the total mean velocity, u_m, w_m, are provided in Fig. 8 for three lower branch solutions (together with the base flow profile) at $\mathrm{Re} = 240$ with increasing permeability. The mean velocity profile u_m is strongly modified by the superposition of the TW, with δ_{99} reaching values as high as $y \approx 15$, compared to the base flow value $y_{99} = 4.605$ (see also Fig. 7). In this sense, the identified TWs can be considered similar to the free-stream TW coherent structures identified in Ref. [41], whose cross-flow energy peaks at $y \approx 12$ (although these solutions are spatially localized and characterized by a shift-and-reflect symmetry). For higher permeability one can observe a larger deflection of the mean profile with respect to the base flow profile. As expected, slight differences are observed between the velocity profiles with $a = 0$ and $a = 3.85 \times 10^{-4}$, whereas the solution with $a = 0.01$ considerably departs from the previous ones. In particular, the spanwise component increases its amplitude especially in the near-wall region, whereas the streamwise one barely changes close to the wall, decreasing in amplitude farther from the wall, up to $y \approx 15$. These contributions can be visualized altogether using the skewed velocity $V_m = \alpha u_m + \beta w_m$, provided in Fig. 9 (left plot) for two lower branch solutions at $\mathrm{Re} = 240$, $a = 0$ and $a = 0.01$ and a near-node solution at $\mathrm{Re} = 231$, $a = 0$. Comparing the red and green curves, related to solutions with different values of a and Re but equal value of $\alpha = 0.129$ (with $\beta = 0.736, 0.707$, respectively), one can notice that the skewed velocity profiles slightly depend on the permeability as well as on the Reynolds number, as far as the chosen values of α and β are close enough. Despite the differences, in the right plot of Fig. 9 one can see that all velocity profiles present several inflection points in the near-wall region going from $2.5 < y < 6$, providing a possible explanation for the mechanism underlying the onset of these unstable solutions at such a low Reynolds number (see also the 2D rendering provided later in Fig. 12).

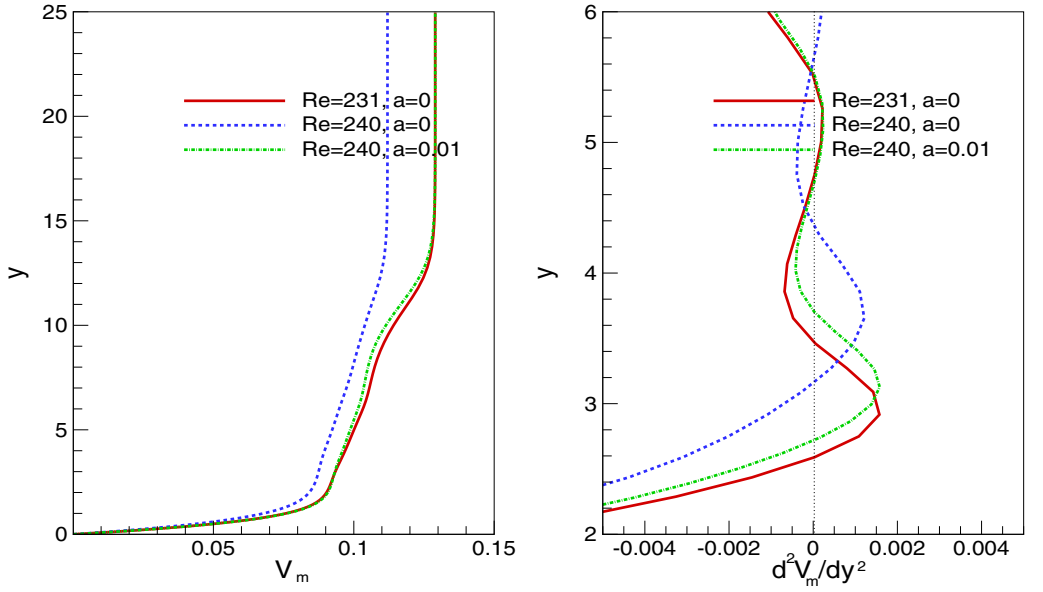

FIG. 9. Skewed velocity V_m (left plot) and its second derivative in the wall-normal direction (right plot) showing a close-up of the region where the inflection points are located. The considered solutions are: $a = 0$, Re $= 231$, $\alpha = 0.129$, $\beta = 0.736$, red solid line, $a = 0$, Re $= 240$, $\alpha = 0.112$, $\beta = 0.68$, blue dashed line; $a = 0.01$, Re $= 240$, $\alpha = 0.129$, $\beta = 0.707$, green dashed-dotted line.

We now focus on the lower branch TWs at Re $= 240$ with $\alpha = \alpha_{SN}$ and $\beta = \beta_{SN}$, indicated by symbols at high c in Fig. 6. Figure 10 shows the wall-normal velocity component of the perturbation for the three considered values of a. Even for a small increase of the permeability there is an observable difference with respect to the zero wall-normal perturbation case ($a = 0$). This applies to the perturbation at $y = 0$ (see the smaller plot in the same figure) as well as in the remaining part of the domain.

The TW solution shown in Fig. 10 reaches finite amplitudes rather close to the wall; then, at a certain wall-normal position $y = y_H$ the solution appears dominated by exponential decay to respect the perturbation-free condition at the free stream. For the TW shown in Fig. 10, this exponential decay sets in at $y = y_H \approx 15$. We analyze the wall-normal variation of the TW solutions in terms of wall units, recalling that a turbulent boundary layer can be divided into three regions: the laminar sublayer ($0 < y^+ < 5$), the buffer layer ($5 < y^+ < 30$) and the log-law region ($30 < y^+ < 1000$), where $y^+ = \check{y}\check{u}_\tau/\check{\nu}$ [with $\check{u}_\tau$ defined above in Eq. (14)]. Plotting the full velocity field of the 3D ASBL-TW solutions (laminar flow plus perturbation) recovered at the node (see Table I) for several stations in x and z, one finds that the finite-amplitude layer close to the wall is contained within the interval stretching from the wall to $y_H^+ \approx 200$–300, thus reaching the log-law region. Whereas, the solutions having λ_z^+ fixed to 100 correspond to lower values of y_H^+ (around 50–100 wall units near the node), as it might have been anticipated since this spanwise wavelength is typical of the coherent structures sustaining the wall cycle.

In laboratory experiments and numerical simulations, turbulence intensities can be measured in terms of the root-mean-square (rms) velocities, the u component as a function of the coordinate y in a domain of length $\lambda_x \times \lambda_z$ being defined as

$$u^2_{\mathrm{rms}}(y) = \frac{1}{\lambda_x \lambda_z} \int_0^{\lambda_x} \int_0^{\lambda_z} (u - u_m)^2 \, dX \, dz. \tag{15}$$

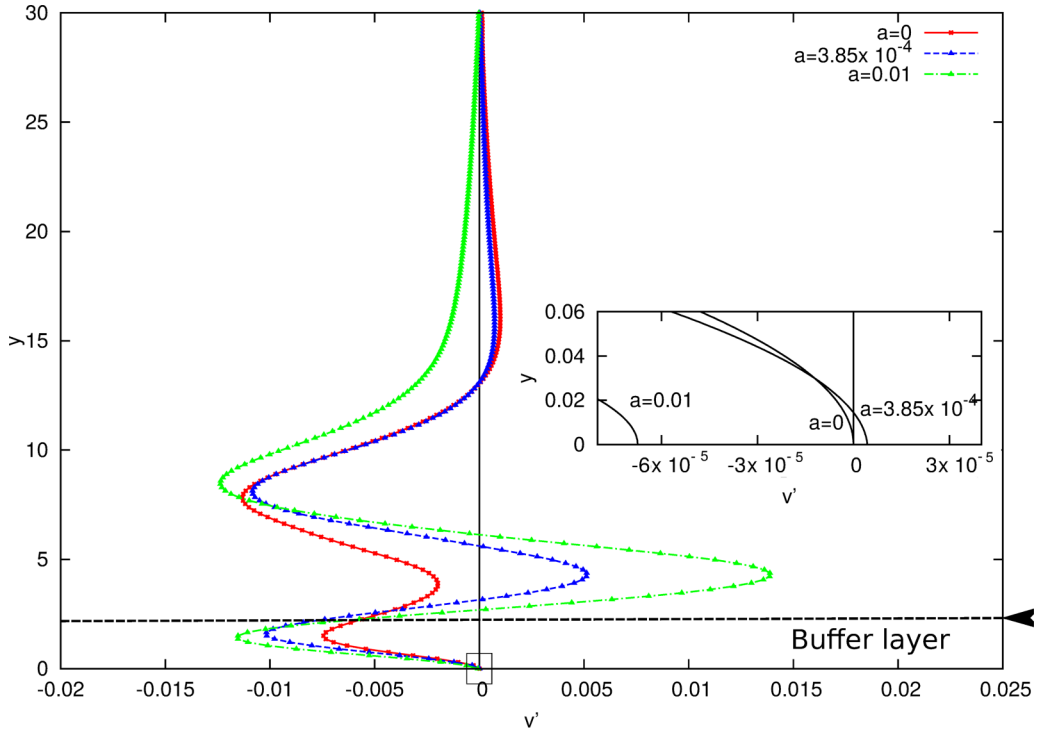

FIG. 10. The v component $v'(X = 0, y, z = 0)$ of the perturbation for the permeabilities $a = 0$ (solid red), 3.85×10^{-4} (blue triangular dashed), and 0.01 (green triangular dashed-dotted) for the lower branch solution near the node at $\mathrm{Re} = 240$ (see the symbols in Fig. 6). The chosen wave numbers are $\alpha = \alpha_{SN}$ and $\beta = \beta_{SN}$ (see Table I). The smaller plot shows a close up of the near-wall region, which extends from the wall to $y = 0.35$: for increasing permeability the v' at $y = 0$ departs from zero to a finite value. The dashed horizontal line allows to identify the buffer layer.

In the case of TWs, u_{rms} measures all spatial fluctuations in x and z with maximum wavelengths λ_x and λ_z equal to $2\pi/\alpha$ and $2\pi/\beta$. Normalizing the rms velocities by the friction velocity $\breve{u}_\tau$ one gets

$$u^+_{\mathrm{rms}}(y) = \left(\frac{1}{\mathrm{Re}}\frac{du_m}{dy}\right)^{-1/2} u_{\mathrm{rms}}(y). \tag{16}$$

Table II presents the maximum value of the rms velocity of the node solutions at $\mathrm{Re} = \mathrm{Re}_{SN}$ showing that the streamwise component dominates by almost an order of magnitude with respect to the other two components. Figure 11 shows the maximum value of the turbulence intensities over the whole domain in y, $\max[v^+_{\mathrm{rms}}]$ versus $\max[u^+_{\mathrm{rms}}]$; see Eqs. (15) and (16). The range in Re and the other parameter values are the same as those given in Fig. 6.

The figure shows that the solutions are characterized by a downstream streaky flow since $\max[u^+_{\mathrm{rms}}] > \max[v^+_{\mathrm{rms}}]$ overall. The u component of the turbulence intensity lies in the same region as that in Ref. [18], which reports $\max[u^+_{\mathrm{rms}}] = 1.59$, $\max[v^+_{\mathrm{rms}}] = 0.66$ for TW solutions of the Blasius flow at $\mathrm{Re} = 500$, and in Ref. [62], where $\max[\overline{u}^+_{\mathrm{rms}}] = 2.7$, $\max[\overline{v}^+_{\mathrm{rms}}] = 0.8$ ($\bar{\cdot}$ indicating time averaging) are recovered in a turbulent channel flow at $\mathrm{Re} = 3300$. The v component for this study is in general lower in comparison, probably due to wall suction. The smaller plot in Fig. 11 shows the rms velocity values as β varies for $\mathrm{Re} = 231$; as the plot indicates, there are no dramatic changes as β departs from $\beta = \beta_{SN}$. Set against the rms values of the equilibrium states and periodic orbits at fixed Reynolds numbers and for various flow configurations summarized in Ref. [37], one can see that the TW solutions in Fig. 11 have weaker values of the rms streamwise

TABLE II. The maximum amplitude of all three component of the rms velocity (scaled with the free-stream speed) for the solutions at the node with no restriction on λ_z^+ (first three lines) and with $\lambda_z^+ = 100$ (last three lines). For $a = 0$, and no restriction set on λ_z^+, the amplitude of the streamwise rms velocity is approximately 14% scaled with the free-stream speed, whereas for the case $\lambda_z^+ = 100$ it slightly lowers to 13%.

a	$\max[u_{\mathrm{rms}}(y)]$	$\max[v_{\mathrm{rms}}(y)]$	$\max[w_{\mathrm{rms}}(y)]$	λ_z^+
0	0.136	0.021	0.014	139
3.85×10^{-4}	0.134	0.022	0.014	131
0.01	0.133	0.023	0.014	134
0	0.125	0.025	0.014	100
3.85×10^{-4}	0.125	0.024	0.014	100
0.01	0.125	0.024	0.014	100

velocity ($\max[u_{\mathrm{rms}}^+] \in [3, 5]$ in Ref. [37] for lower branch states, whereas $\max[v_{\mathrm{rms}}^+] \in [0.15, 0.4]$). For comparison, the peak values of the time-averaged rms velocities obtained by DNS of turbulent asymptotic suction boundary layer flows are also reported for the present study at $\mathrm{Re} = 240$ with $a = 0, 0.01$ (square symbols; see also Sec. III B) and for the investigation in Ref. [51] (star symbol)

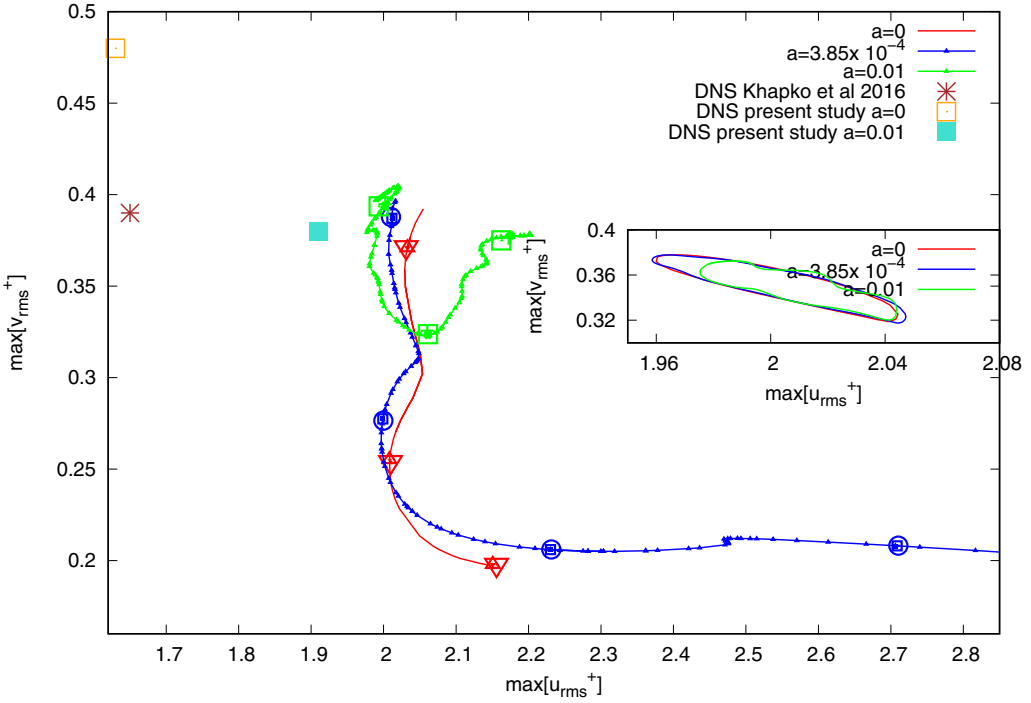

FIG. 11. Main figure: Root-mean-square values of the TW represented by $\max[v_{\mathrm{rms}}^+]$ vs $\max[u_{\mathrm{rms}}^+]$ with Re changing along the curves. The flow cases considered are those shown in Fig. 6, and the symbols are those used in the same figure to confirm convergence. Insert: The same velocities as in the big plot with β changing along the curves for $\mathrm{Re} = 231$ (close to Re_{SN}). The value of α is $\alpha(a = 0) = 0.129$ (close to α_{SN}; see Table I), $\alpha(a = 3.85 \times 10^{-4}) = 0.128$ and $\alpha(a = 0.01) = 0.129$. The peak values of the time-averaged rms velocities obtained by DNS of turbulent asymptotic suction boundary layer flows are also reported for three selected cases: present study at $\mathrm{Re} = 240$ with $a = 0$ (orange square) and $a = 0.01$ (cyan square) and Ref. [51] at $\mathrm{Re} = 280$ (red star).

TABLE III. The main parameters characterizing the TWs which have been analyzed by linear and nonlinear DNS as well as the number of grid points and the recovered growth rate σ of the leading unstable mode for each simulation.

a	α_{SN}	β_{SN}	Re	c	y_∞	N_x	N_y	N_z	σ
0	0.112	0.680	240	0.78	25	401	101	61	0.012
3.85×10^{-4}	0.128	0.726	240	0.76	30	301	121	51	0.016
0.01	0.129	0.707	240	0.76	30	301	136	41	0.076
0	0.112	0.680	300	0.88	30	401	121	61	0.021
3.85×10^{-4}	0.128	0.726	300	0.87	30	401	121	61	0.021
0.01	0.129	0.707	300	0.72	30	401	136	61	0.096

at $\mathrm{Re} = 280$ in large numerical domains. For $a = 0.01$ the rms velocity values obtained by DNS are reasonably close to those characterizing the TW solutions, indicating that considering a nonzero perturbation condition at the wall might be crucial for correctly describing the nonlinear dynamics of the flow. Increasing the permeability to $a > 0.01$ might give a better match; however, this is not carried out due to high requirement of computer memory already for $a = 0.01$. A way of finding different solutions, possibly associated to higher turbulent intensities, would be to search for 3D solutions bifurcating away from the Tollmien-Schlichting waves found in Ref. [39].

The stabilizing effects of suction on the flow in a boundary layer constrained on a 2D framework is evident when comparing the linear and nonlinear stability limit in the Reynolds number for the 2D BBL and the ASBL (zero permeability $a = 0$). The linear stability limit is $\mathrm{Re}_c^{BBL} \approx 520$ [44,45], whereas $\mathrm{Re}_c^{ASBL} \approx 54\,400$ [42–44]; the minimum Reynolds number at which 2D nonlinear states are found is $\mathrm{Re}_{SN}^{BBL} = 510$, whereas $\mathrm{Re}_{SN}^{ASBL} = 3168$ [39,58]. This implies that wall suction delays growth of small amplitude perturbations, as well as the emergence of alternative 2D finite-amplitude solutions of the Navier-Stokes equations, to much higher Re. When considering 3D nonlinear alternative solutions, we have shown in this study that for the ASBL they exist from $\mathrm{Re}_{SN} = 225$, whereas for the BBL from $\mathrm{Re}_{SN} = 496$ [18]; see also Table I. For the 3D case it thus seems that suction renders the flow more nonlinearly unstable compared to the BBL, contradicting the stabilizing effects found when restrained to a 2D configuration. Focusing on the flow close to the wall the present study shows that a model of the wall porosity should be used for allowing wall-normal perturbations at the wall. Even though similar values of $\mathrm{Re}_{SN}(a)$ are obtained, discernible differences are seen when looking at the shape of the TWs already for small values of a set against the zero perturbation case $a = 0$.

However, the role of these TW solutions in transition and turbulence remains to be investigated: one might wonder whether they are pretransitional flow states multiplying in number as Re increases away from Re_{SN}, and whether they serve as a part of the transition process, or they are merely nonlinear states of the Navier-Stokes equations with no particular physical meaning. Reference [63] demonstrates the connection between nonlocalized TWs and localized periodic orbits, showing that more complex states can be discovered using TWs as a base flow. The large differences in Re_{SN} of the 2D waves and the lower limit of sustained turbulence Re_g implies that 2D TW solutions for the ASBL may not fit into the classical route of boundary layer transition at low Re. Although the classical transition scenario initiated by 2D Tollmien-Schlichting waves is undoubtedly observed in the flow over aircraft wings and in many turbomachinery applications (for instance, low-pressure turbines), abrupt transition can be observed even at low Reynolds number, justifying the search for saddle nonlinear solutions at $\mathrm{Re} \ll \mathrm{Re}_c$. For the boundary-layer flow considered here, the values of Re_{SN} of the 3D states and Re_g almost coincide, suggesting that 3D waves play part in the turbulence transition at low Reynolds numbers. The rather low rms velocity values indicate that the lower branch 3D TWs might belong to a family of solutions sitting in a pretransitional domain of the state space. To further the understanding of the importance of the TWs found here, linear and nonlinear numerical simulations are carried out in the following section.

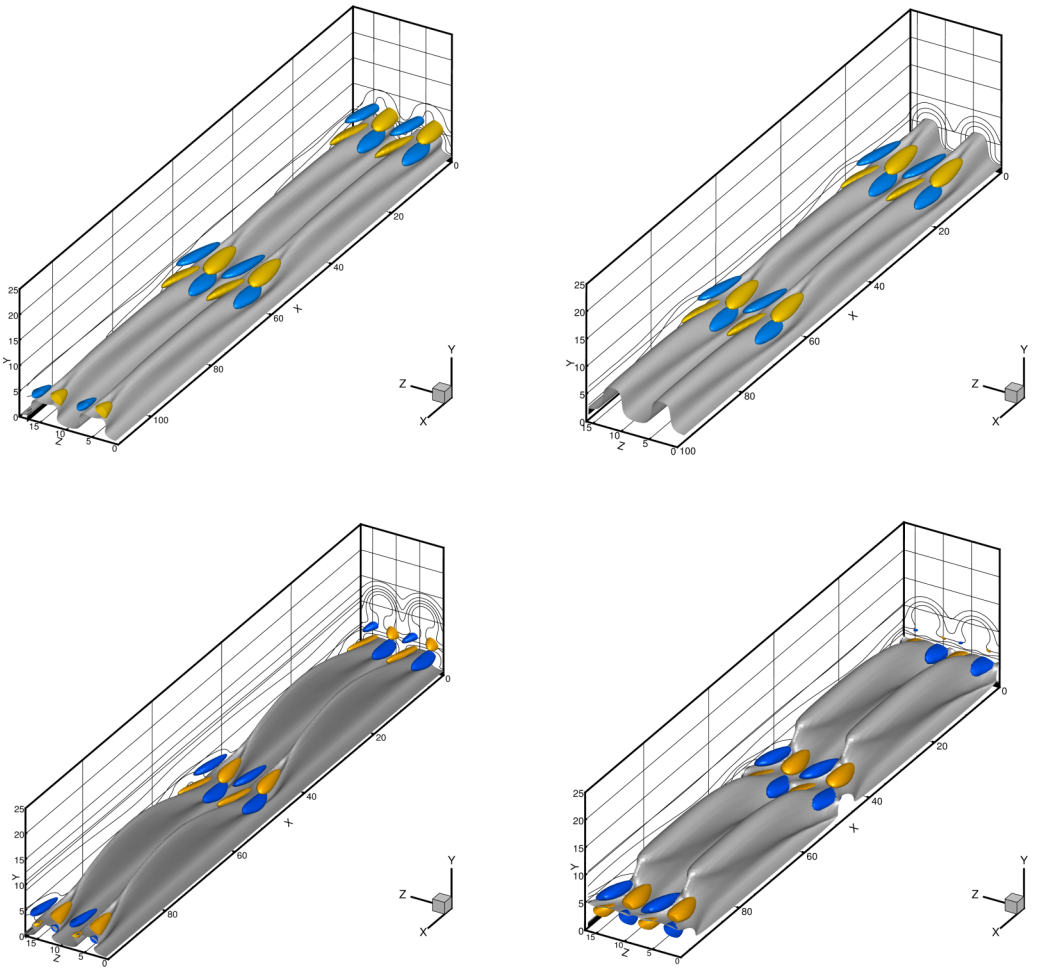

FIG. 12. Three-dimensional rendering of the lower branch TW obtained at Re = 300 for the permeabilities $a = 0$ (top left), 3.85×10^{-4} (top right), 0.01 (bottom left) and at Re = 240 $a = 0.01$ (bottom right). The chosen wave numbers are $\alpha = \alpha_{SN}$ and $\beta = \beta_{SN}$ (see Table I). The gray isosurfaces and the solid lines show the instantaneous streamwise velocity (for the isosurfaces, $u = 0.8$ for $a \leqslant 3.85 \times 10^{-4}$, $u = 0.65$ for $a = 0.01$); whereas the yellow and blue surfaces provide the positive and negative spanwise velocity components ($w = \pm 0.015$ for $a \leqslant 3.85 \times 10^{-4}$, $w = \pm 0.025$ for $a = 0.01$). The mean flow moves towards increasing values of x.

B. The linear and nonlinear flow evolution starting from TWs

With the aim of studying the linear and nonlinear dynamics of the flow in the vicinity of the TWs presented above, we have selected six lower branch solutions reported in Table III together with the corresponding grid points for the DNS, for two different values of the Reynolds number, Re = 240, 300, and the three values of the permeability considered before. A 3D plot of the selected solutions for Re = 300, $a = 0, 3.85 \times 10^{-4}$, 0.01 and Re = 240, $a = 0.01$, is provided in Fig. 12. One can notice the modulated streaky structures (gray surfaces representing the streamwise instantaneous velocity) as well as the spanwise velocity components (yellow and blue) placed in the regions of largest gradient of the streaks. The solutions for small (or zero) permeability are very similar to each other and present a mild streamwise modulation (top frames), which increases considerably in strength for the case at $a = 0.01$ (bottom frames), for both the considered values of

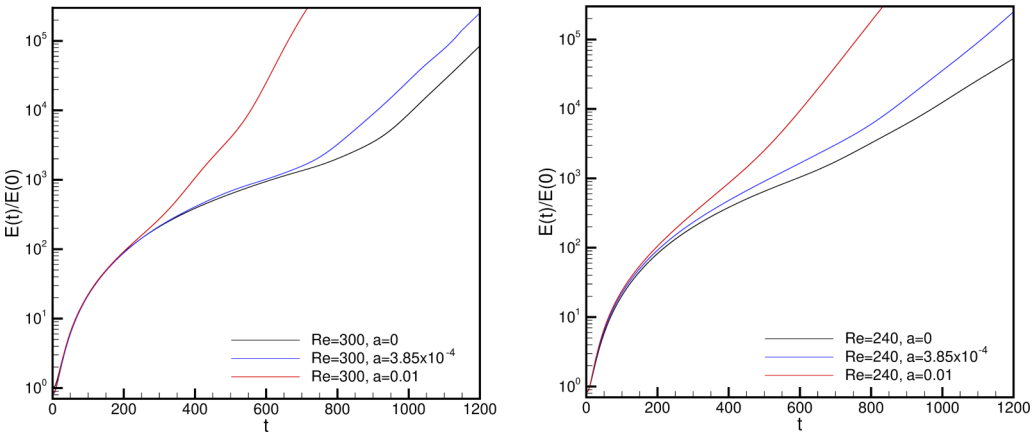

FIG. 13. Energy gain associated with the perturbations of the TWs at Re = 300 (left) and Re = 240 (right), for the three considered values of the permeability as recovered by linearized DNS. The curves correspond to $a = 0$ (black), $a = 3.85 \times 10^{-4}$ (blue), and $a = 0.01$ (red); see legend.

Re. Despite the different symmetry and space localization, the structure of these solutions recalls that of the localized TW found in Ref. [41], composed by streaks reaching a wall-normal position of order 10, flanked by inclined streamwise-localized vortices. Injecting a random perturbation $\mathbf{u}''$ not respecting the reflect symmetry onto the selected TW solutions and measuring its linear evolution in time by means of the perturbation energy,

$$E(t) = \frac{1}{2V}\int_V [(u'')^2 + (v'')^2 + (w'')^2](t)dV, \tag{17}$$

where V is the volume of the computational domain, we obtain the energy gain curves in Fig. 13. One can observe that, after an initial algebraic growth, the energy gain curves follow an exponential behavior characterized by a growth rate which increases with the permeability a and the Reynolds number. Evaluating the slope of the energy gain curves is possible to measure the value of the growth rates, which are reported in Table III for each of the considered case. The corresponding steady unstable modes are plotted in Fig. 14 for Re = 300, $a = 0$ (left frame) and $a = 0.01$ (right frame). The unstable modes are characterized by localized patches of perturbations placed right downstream of the region where the streaks are bent (as visualized by the solid lines representing the streamwise instantaneous velocity). The unstable modes appear to break the reflect symmetry of the TWs, presenting streamwise velocity perturbations of opposed sign at the flanks of the streaks.

These perturbations have a typical size which is comparable with that of the region where high-amplitude spanwise velocity components of the TW itself are found. This indicates that the physical mechanism at the origin of these unstable modes might be the bending of the streaky structures themselves, which will increase in time in a localized region, inducing the break up of the TW solution. However, transition might be as well be due to the total shear exceeding a critical value, irrespective of how much streaks are bent. One can also observe that in the case having a finite permeability, the unstable mode extends towards higher values of y, indicating that the destabilization is taking place on the whole solution and not close to the plate.

The unstable modes described above are then used to initialize nonlinear DNS with different values of the initial energy, in order to ascertain the possibility of a turbulent transition starting from these TW solutions. Values of $E(0)$ ranging from 10^{-3} to 10 have been considered. Figure 15 shows the energy $E(t)$ of the perturbations with $E_0 = 10^{-3}, 10^{-1}, 10$ for Re = 240, $a = 0$ (left frame). In all the cases, the energy increases exponentially and then saturates to an average value which is typical of a turbulent behavior. Changing the value of the permeability does not modify this

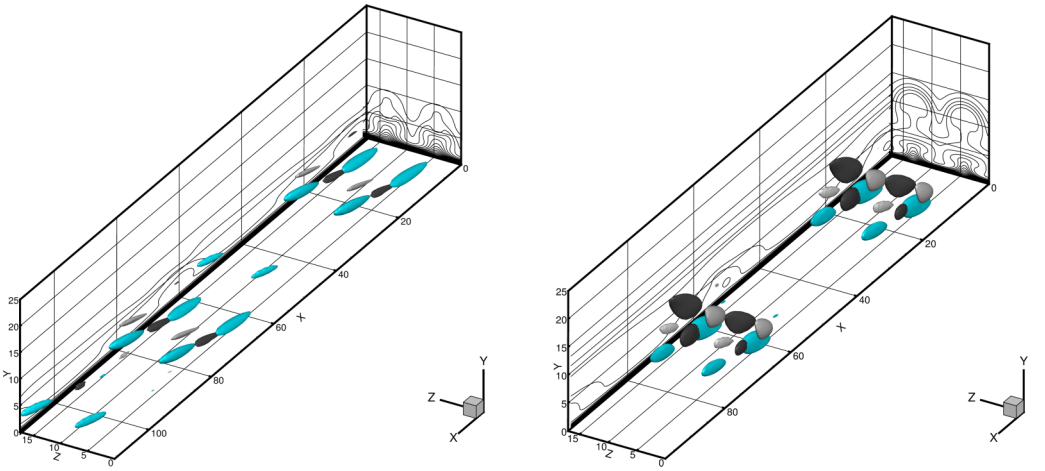

FIG. 14. Three-dimensional rendering of the most unstable modes of the lower branch TW obtained at Re = 300 for the permeabilities $a = 0$ (left) and $a = 0.01$ (right). The chosen wave numbers are $\alpha = \alpha_{SN}$ and $\beta = \beta_{SN}$ (see Table I). The solid lines show the TW instantaneous streamwise velocity; whereas the light and dark gray isosurfaces show the instantaneous streamwise velocity perturbation of the TW ($u'' = -0.35u''_{\max}$) and blue ones indicate the spanwise velocity component of the perturbation ($w'' = \pm 0.55w''_{\max}$). The mean flow moves towards increasing values of x.

result, since transition to turbulence starting from the TW plus its unstable mode is observed in all of the considered cases (right frame). Figure 16 provides four snapshots extracted from the direct numerical simulation for Re = 240 and $a = 0$ for times $t = 100, 300, 500, 700$ starting from the instant of injection of the unstable mode with energy $E_0 = 10$. In the top left frame one can observe the effect of the unstable mode on the streaky structures, which show now several modulations with small wavelength. At $t = 300$, some points of extreme bending of the streaks can be observed, which induce the formation of localized patches of cross-flow velocity components which break the elongated structure of the TW ($t = 500$). Finally, at $t = 700$, the streaks have been completely broken up and a chaotic behavior have already settled in the flow.

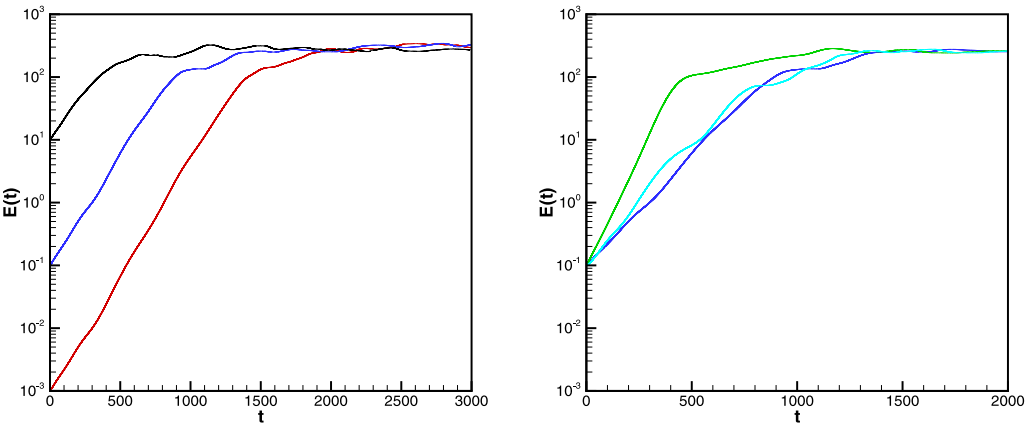

FIG. 15. Nonlinear time evolution of the energy of the modal perturbation of the TW solutions at (left) Re = 240, $a = 0$ for initial energies $E_0 = 10^{-3}, 10^{-1}, 10$, from bottom to top, and (right) $E_0 = 10^{-1}$ and $a = 0, 3.85 \times 10^{-4}, 0.01$ (right, from bottom to top) obtained by DNS (notice that the blue lines in the left and right frame represent the same case).

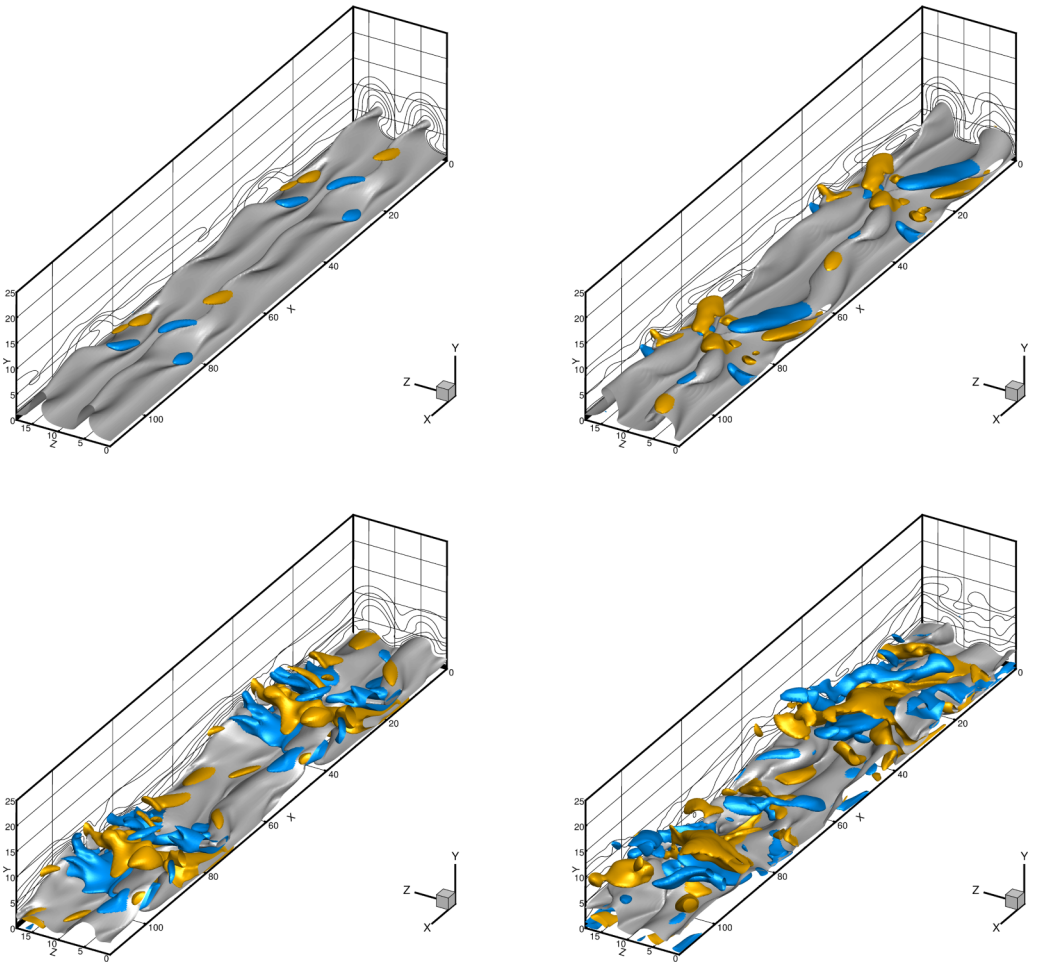

FIG. 16. Snapshots extracted from the DNS of the transition to turbulence initiated by the TW at Re = 240, $a = 0$ plus its most unstable mode at $t = 100$ (top left), $t = 300$ (top right), $t = 500$ (bottom left), and $t = 700$ (bottom right). The gray isosurfaces and the solid lines show the instantaneous streamwise velocity (for the isosurfaces, $u = 0.75$); whereas the yellow and blue surfaces provide the positive and negative spanwise velocity components ($w = \pm 0.045$ for $t = 100$, $w = \pm 0.025$ for $t > 100$). The mean flow moves towards increasing values of x.

To ensure that the observed chaotic behavior indicates indeed transition to turbulence, we have computed the time average of the velocity components averaging them over 1000 time units after the initial transient has passed. Figure 17(a) shows the time-averaged mean streamwise velocity profiles in friction units plotted with respect to y^+ (black solid line). One can observe that in the near-wall region the mean profile is superposed to the modified linear law (red dashed line) provided in Ref. [64] for the asymptotic suction boundary layer, namely,

$$U^+ = \frac{1}{V_0^+}(\exp^{V_0^+ y^+} - 1). \tag{18}$$

Whereas, in the outer region the profile is close to an empirical log law $U^+ = \frac{1}{\kappa} \ln y^+ + A$, as also observed in a recent experiment [65]. The profile slope, $\kappa \approx 0.82$, as well as the value of $A \approx 7$, are different from those recently provided in Ref. [51], probably because of the much smaller domain

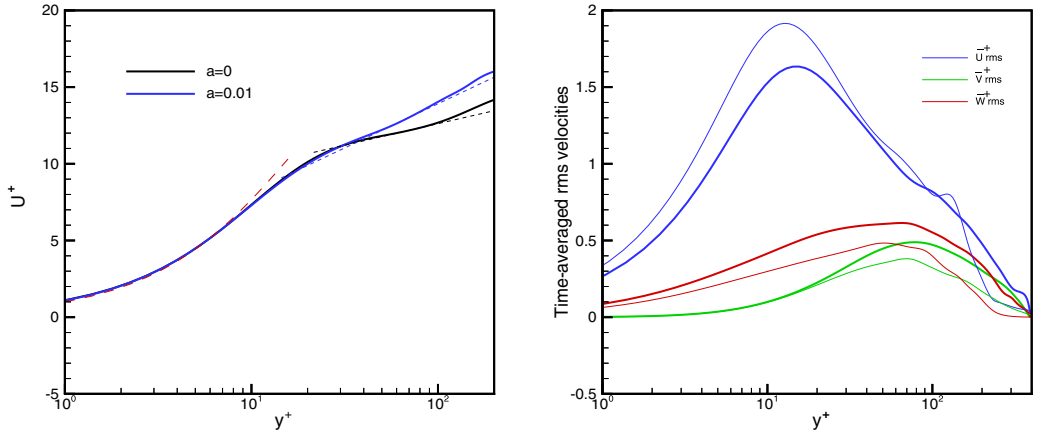

FIG. 17. Turbulent flow statistics extracted from the DNS for $\mathrm{Re} = 240$ after the initial transient. (Left) Time-averaged mean flow $\overline{u}^+$ vs y^+ for $a = 0$ (black) and $a = 0.01$ (blue), fitted by the modified linear law proposed by Ref. [64] (red long dashed line) and by the empirical log law with different values of k and A (short dashed lines). (Right) Time-averaged rms velocity profiles, $\overline{u}^+_{\mathrm{rms}}$, $\overline{v}^+_{\mathrm{rms}}$, $\overline{w}^+_{\mathrm{rms}}$ computed with respect to the mean flow vs y^+ for $a = 0$ (thick lines) and $a = 0.01$ (thin lines).

we have used in the wall-normal and spanwise direction, which does not allow the formation of large-scale coherent structures reaching the outer region. Indeed, one can notice that at large values of y^+ the profile plotted in Fig. 17(a) overshoots the log law, similarly to what has been observed in Ref. [51] in the case where large-scale structures are artificially damped. Similar observations can be made on the long-time average of the rms profiles versus y^+ provided in Fig. 17(b), where the rms values are computed with respect to the mean flow (instead of u_m) for a better comparison with the literature data. The time-averaged rms velocity profiles, $\overline{u}^+_{\mathrm{rms}}$, $\overline{v}^+_{\mathrm{rms}}$, $\overline{w}^+_{\mathrm{rms}}$, are very similar in shape and value to those reported in Ref. [51] for rather larger values of the Reynolds number ($\mathrm{Re} \geqslant 270$), although the rapid drop of the profiles at large y^+ is similar to that observed by the same

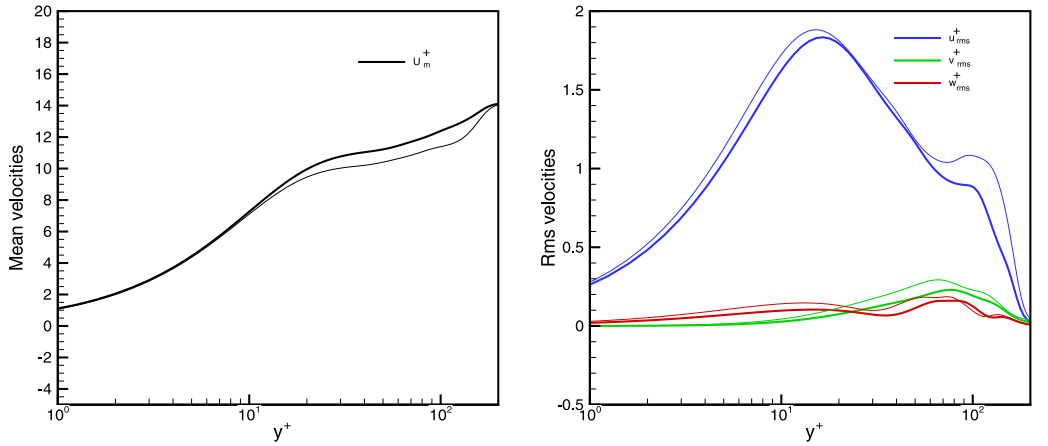

FIG. 18. Mean and rms velocity profiles of the TW used for producing the turbulent flow statistics in Fig. 17 ($\mathrm{Re} = 240$) plotted in friction units vs y^+. Left plot: Mean velocity profile for $a = 0$ (thick line) and $a = 0.01$ (thin line). Right plot: RMS velocity profiles u^+_{rms}, v^+_{rms}, w^+_{rms} for the lower branch solutions at $a = 0$ (thick lines) and $a = 0.01$ (thin lines).

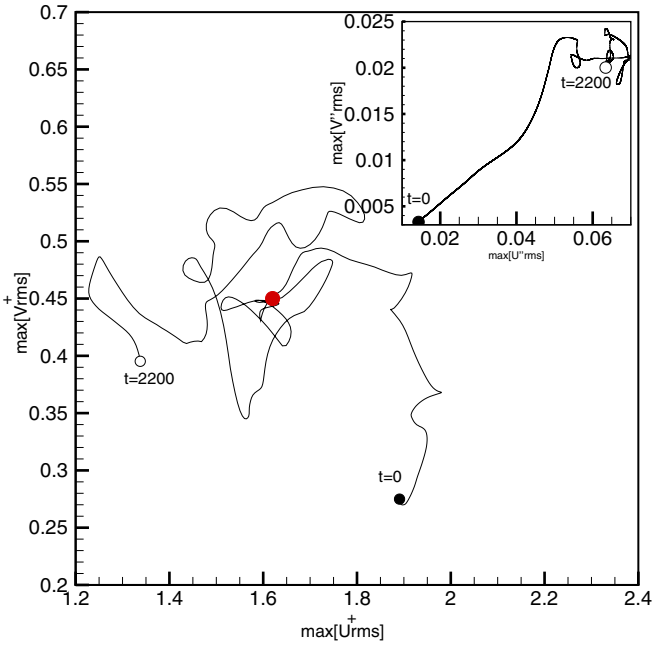

FIG. 19. State portraits on a $\max[u^+_{\rm rms}]$ vs $\max[v^+_{\rm rms}]$ plane. The trajectory starts from the selected TW at $\mathrm{Re} = 240$, $a = 0$, plus its most unstable mode with initial energy $E_0 = 10$, at $t = 0$ (black dot) and evolves up to $t = 2200$ (white dot). The red dot indicate the values of $\max[u^+_{\rm rms}]$ and $\max[v^+_{\rm rms}]$ in the turbulent regime. In the inner plot the same trajectory is shown in a $\max[u''_{\rm rms}]$ vs $\max[v''_{\rm rms}]$ state portrait where only the perturbation to the TW has been considered for computing the rms.

authors in the presence of large-scale damping. The same statistics are also provided in Fig. 17 for the turbulent flow with $\mathrm{Re} = 240$, $a = 0.01$. Although a general law cannot be extracted due to limited domain lengths, one can observe that, varying the wall permeability, the velocity profile remains exactly the same close to the wall, following the modified linear law provided in Eq. (18), whereas the empirical log law at the outer scale appears to change its slope. In particular, much lower values of κ and A ($\kappa = 0.4$, $A = 2.4$, the value of κ being close to that recovered for the BBL) are recovered for $a = 0.01$ with respect to the case at vanishing wall permeability. Concerning the rms velocity profiles, larger (smaller) values of the streamwise (cross-flow) rms velocities are recovered, confirming that varying the wall permeability affects the dynamics of the flow structures from a quantitative point of view. For comparison with the turbulent profiles, we provide in Fig. 18 the mean and rms velocity profiles of the two considered solutions at $\mathrm{Re} = 240$ expressed in friction units versus y^+. As anticipated, the considered solutions present considerable differences with respect to the turbulent profiles, since lower branch solutions are more representative of a transitional than a turbulent state.

The time evolution of the peak values of the rms velocities is further analyzed by plotting the flow trajectory between $t = 0$ and $t = 2200$ on a $\max[u^+_{\rm rms}]$ versus $\max[v^+_{\rm rms}]$ plane in Fig. 19. The origin of the trajectory, which is composed of the TW plus a rather small perturbation, is characterized by large values of $\max[u^+_{\rm rms}]$ and smaller values of $\max[v^+_{\rm rms}]$, similarly to what has been found in Refs. [37,66] for many lower branch exact coherent states in canonical shear flows. The nonlinear time evolution brings the trajectory towards a region of the state space where $\max[u^+_{\rm rms}]$ decreases and $\max[v^+_{\rm rms}]$ increases, reaching values close to those of the upper branch exact coherent states ($\max[v^+_{\rm rms}] > 0.45$ for upper branch states according to Refs. [37,66]). The trajectory wanders around this region for a rather long time, suggesting that the flow has reached the chaotic saddle

constituted by many neighboring upper branch solutions, which attract the trajectory along their stable manifolds and then repel it along their unstable directions. This is confirmed by looking at the state portrait in an alternative plane given by the $\max[u''_{\mathrm{rms}}] - \max[v''_{\mathrm{rms}}]$ plane where only the perturbations of the TW have been considered for computing the rms (inner plot of Fig. 19). It is clear that the trajectory quickly escapes from the lower branch solution, since the perturbation of the TW increases very quickly until reaching a region rather far from the initial solution where it begins to oscillate around a mean value. A similar behavior has been observed for different values of a and Re, indicating that the computed TWs may constitute an important building block for transition to turbulence in the considered flow.

IV. CONCLUSIONS

Three-dimensional traveling waves (TWs) in an asymptotic suction boundary layer (ASBL) are studied in order to get insight on their role in state space at low values of the Reynolds numbers Re. To model the variation of the wall-normal perturbation at the wall as a consequence of the pressure gradient applied to engender the wall suction, the Darcy's law has been used. The effect of different wall permeabilities a on the TW solutions as well as their instability is investigated.

Nonlinear solutions having a reflect symmetry in the spanwise coordinate are computed down to the node at $\mathrm{Re} = \mathrm{Re}_{SN} = 225$ (the Reynolds number being based on the displacement thickness), where this minimum point emerges subcritically. To our knowledge, the value of Re_{SN} obtained in this work is considerably lower than the lowest value for which exact coherent states have been recovered in the literature for the asymptotic suction boundary layer, as well as for the BBL. This indicates that the presence of wall suction might be destabilizing in a nonlinear framework, leading to the self-sustainment of finite-amplitude saddle solutions at very low values of the Reynolds number.

The TWs close to the saddle node reach the log-law region of an equivalent turbulent boundary layer. Looking at the rms of the velocity components reveals that the solutions near Re_{SN} are characterized by streamwise-modulated streaks. Comparing to invariant solutions computed elsewhere for other flows shows that the TWs computed herein are weaker in one or both the streamwise- and wall normal components, probably due to the presence of suction at the wall. These rms velocities change with Re, although remaining lower than those found for other shear flows. Moreover, it appears that increasing the wall permeability does not change the value of Re_{SN} much. The effect of changing a is discernible when mapping out the TW in Re away from the global minimum point, since increasing it renders the TW more nonlinear, providing notable differences in the amplitude and wave speed of the solutions, whereas the bifurcation curves at different permeabilities collapse when choosing their spanwise wavelength according to the well-known spacing $\lambda^+ \approx 100$ recovered between streaks in wall turbulence. The present study suggests that the influence of the wall porosity on the wall-normal perturbation should be taken into account when computing nonlinear solutions of the Navier-Stokes equations. In fact, even for small (but finite) values of a noticeable differences are recovered with respect to the case $a = 0$, for which the wall-normal perturbation is considered to vanish at the wall, as currently assumed in the literature.

As in the case of the circular pipe flow, the TWs survive down to Reynolds numbers below the critical one for sustained turbulence obtained for large computational domains. This is a sign that the TWs may be a prerequisite of an increasing complexity in state space before transition sets in with the subsequent occurrence of turbulent flow at a later stage. Provided that the permeability of the porous wall is kept below a certain threshold, earlier studies show that wall suction delays the growth of both linear and nonlinear 2D states to much higher Re, compared to the BBL flow (with no permeable wall allowing suction). For the 3D case considered here, it is shown that flow suction renders the flow more nonlinearly unstable compared to the BBL flow, being $\mathrm{Re}_{SN}^{ASBL} = 225$ and $\mathrm{Re}_{SN}^{BBL} = 496$ [18]. Thus, it is clear that suction is very efficient only in suppressing waves of very low amplitudes. Hence, no firm conclusion can be made whether or not suction can be used to prevent transition to turbulence, since at values of the Reynolds number slightly larger than Re_{SN}

(namely, Re = 240), transition to turbulence is observed when departing from the 3D TW along its unstable manifold.

Finally, the route to turbulence at Re = 240 has been studied by visualizing the breakdown of the modulated streaks characterizing the TW and by analyzing the variation in time of the rms velocity values using a state portrait. As in other shear flows, the maximum wall-normal rms velocity increases and the streamwise one decreases when passing from the considered lower branch TW to the chaotic saddle. Moreover, turbulent flow statistics have been extracted for different values of a, showing that the wall permeability has a non-negligible effect on turbulent flow features such as the streamwise velocity peak and the slope of the log law in the outer region.

Further studies will aim at extending these results to 3D TW having different symmetries, which might further lower the recovered value of Re_{SN} and complete the picture of transition to turbulence starting from TW solutions. Also, an attempt to compute localized exact coherent states for values of the Reynolds number lower than the critical one for sustained turbulence, will be of a great interest for clarifying the role of these invariant sets for the onset of turbulent transition.

ACKNOWLEDGMENTS

The financial support of a European Re-integration Grant (ERG) No. 268265 is gratefully acknowledged (H.W.). The authors would like to thank A. Bottaro for the fruitful discussions which inspired the main idea of the present paper. The authors also wish to thank the personnel at the library of Luleå University of Technology, Sweden, for efficient help and for their availability.

APPENDIX: THE FORCING FUNCTION AND THE SEARCH OF TRAVELING WAVES

For computing TWs at rather low Reynolds number, a forcing function $\boldsymbol{f}(y,z)$ is added to the Navier-Stokes equations. To find a suitable expression for the forcing, a method based on the self-sustaining process (SSP) proposed in Ref. [67] has been used. The SSP has proved useful for discovering numerical nonlinear solutions to the Navier-Stokes equations in various configurations (see Refs. [11,12,14,15,68–70], among others). The main objective is to bring the forcing to zero for a $\boldsymbol{u}'$ having finite amplitude. The definition of $\boldsymbol{f}$ is explained further below. The final equations governing the perturbation with the $\boldsymbol{f}$ included are

$$\boldsymbol{u}'_t + \boldsymbol{\nabla} p' - \frac{1}{\mathrm{Re}}\nabla^2\boldsymbol{u}' + (U\cdot\boldsymbol{\nabla})\boldsymbol{u}' + (\boldsymbol{u}'\cdot\boldsymbol{\nabla})U + V\boldsymbol{u}'_y + \epsilon\boldsymbol{u}'\cdot\boldsymbol{\nabla}\boldsymbol{u}' - \boldsymbol{f} = \boldsymbol{0}. \tag{A1}$$

The forcing function is defined as $\boldsymbol{f}(y,z) = f_v(y,z)\mathbf{j} + f_w(y,z)\mathbf{k}$, where the functions f_v and f_w appear in the v-momentum and the w-momentum equations, respectively. These forcing functions are used for driving an instantaneous x-independent cross-flow, corresponding to the Fourier mode with $b = 0$, represented by $\tilde{\boldsymbol{V}}(y,z) = \tilde{V}(y,z)\mathbf{j} + \tilde{W}(y,z)\mathbf{k}$, whereas the x (and time) -dependent part of the perturbation is defined as $\breve{v}(t,x,y,z) = \sum_{b,j} v^{(bj)}(y)\exp[Ib\alpha(x-ct)]\exp(Ij\beta z)$ with $b \neq 0$. To lower the size of the system of equations we bring the Navier-Stokes equations to a reduced pressure-free form governing the time-dependent part of the perturbation $\breve{v}(t,x,y,z)$ and $\breve{w}(t,x,y,z)$ as well as the instantaneous streamwise velocity $\tilde{U}(y,z)$ and the stream function $\tilde{\psi}(y,z)$ (both having $b = 0$). The time-dependent velocity component $\breve{u}(t,x,y,z)$ can be then easily recovered using the continuity equation. The stream function $\tilde{\psi}(y,z)$ represents the x-independent cross-flow through the relations $\tilde{V}(y,z) = \partial_z\tilde{\psi}(y,z)$ and $\tilde{W}(y,z) = -\partial_y\tilde{\psi}(y,z)$. The equation of the time-dependent stream function $\breve{\psi}(t,y,z)$ is used for defining the forcing function and deserves some extra attention. This equation is derived by accounting for the x-average (overbar) of Eq. (6); taking $\mathbf{i}\cdot\boldsymbol{\nabla}\times\overline{(6)}$ we arrive at

$$-\frac{\partial}{\partial t}\nabla^2\breve{\psi} = -\frac{1}{\mathrm{Re}}\nabla^4\breve{\psi} + \mathcal{N}(\breve{\psi}) + \overline{\mathcal{N}(\breve{\boldsymbol{u}})}, \tag{A2}$$

where $\mathcal{N}$ represents the nonlinear terms. The purpose of accounting for the time-dependence of $\breve{\psi}$ will now be shown. The forcing is defined by the term on the left-hand side of Eq. (A2). In order to describe how it is constructed, we set the time-derivative term $\frac{\partial}{\partial t}\nabla^2\breve{\psi}$ equal to $\frac{\partial}{\partial t}\nabla^2 g(t)\psi_f(y,z)$, where ψ_f is a function to be determined for defining the forcing that drives the $\tilde{\psi}(y,z)$. When looking at the fully linearized $\breve{\psi}$ equation (A2), the $g(t)$ will merely give rise to an amplitude f_A of the time-derivative term due the exponential behavior in time of the linear solution. Therefore the final expression of the forcing is $f(y,z) = f_A\nabla^2\psi_f(y,z)$. Taking into account the definition of the forcing and mimicking Eq. (A2) we get

$$-f_A\nabla^2\psi_f(y,z) = -\frac{1}{\mathrm{Re}}\nabla^4\tilde{\psi} + \mathcal{N}(\tilde{\psi}) + \overline{\mathcal{N}(\breve{\boldsymbol{u}})}. \tag{A3}$$

Starting from small amplitudes f_A, the solution of $\tilde{\psi}$ remains close to the linear one, however with increasing amplitude the term $\mathcal{N}(\tilde{\psi})$ becomes progressively important. For driving the solutions we construct and use an analytical stream function $\psi_f(y,z)$ defining the forcing on the basis of physical considerations. In particular, we use the continuity equation to determine a suitable function for describing x-independent rolls $\tilde{\boldsymbol{V}}(y,z) = \tilde{V}(y,z)\mathbf{j} + \tilde{W}(y,z)\mathbf{k}$, which satisfy the no-slip boundary condition at $y = 0$ and the asymptotic condition at the outer edge of the computational domain at $y = y_\infty$. Then, using the given relation between $\tilde{\psi}(y,z)$, $\tilde{V}(y,z)$, and $\tilde{W}(y,z)$ we can define the stream function as

$$\psi_f(y,z) = -\mathrm{Im}[y^2\cos(b_2 y)e^{-\beta y}e^{I\beta z}]. \tag{A4}$$

This expression has already been successfully used in Ref. [18] for finding finite-amplitude solutions in the BBL flow. The cosine expression is chosen in order to set the dependency in y with the constant b_2 determining its periodicity. In this study, we have set $b_2 = 0.5$. However, the results of the previously mentioned study of the BBL flow indicate that different values of b_2 will yield the same solution when $f_A = 0$. The term y^2 is used since $\psi_f(y,z)$ is linked to the cross-flow, thus we need to satisfy both the Neumann and the Dirichlet boundary conditions at $y = 0$. The exponential $e^{-\beta y}$ sets the correct asymptotic decay in the free stream. To take into account the imposed symmetry [see Eq. (11)] we consider only the imaginary part of the previously described function. Then, in order to compute approximate solutions (forced at $f_A \neq 0$) of the Navier-Stokes equations, we linearize them with respect to the time-dependent part $\breve{u}$ and find solutions to the instantaneous part $\tilde{U}(y,z)$ and the $\tilde{\psi}(y,z)$ driven by the $f(y,z)$. Subsequently, $\breve{v}(t,x,y,z)$ and $\breve{w}(t,x,y,z)$ are obtained solving a linear eigenvalue problem where the instantaneous part plus the laminar flow are used as a new base flow. When a real eigenvalue $c = c_r$ is recovered, we obtain an approximate solution ($\breve{v}$, $\breve{w}$, $\tilde{U}$, $\tilde{\psi}$; $f_A \neq 0$) at a bifurcation point, which is the prior condition for starting the search of finite-amplitude solutions residing at vanishing f_A. This approximate solution, composed of the x-independent part and the first Fourier mode in x, is supplied to a nonlinear solver called PITCON, a Fortran subroutine utilizing a Newton-Raphson technique, developed by [71,72]. In this way, the Navier-Stokes equations are solved iteratively until convergence is obtained, recovering a nonlinear solution. The governing equations can be defined by the vector $\boldsymbol{F}$. In order to solve the equations iteratively one needs to formulate the gradient of $\boldsymbol{F}$ represented by the Jacobian matrix $\boldsymbol{J}$. In detail the PITCON subroutine solves the Navier-Stokes equations iteratively $n = 0, \ldots, N$ as shown in Eq. (A5). The nonlinear solutions are traced out in the continuation parameter Ω by supplying the algorithm with an initial guess, i.e., the previous converged solution at Ω-$\Delta\Omega$, then taking a step forward in Ω and restarting the iteration procedure as follows:

$$-\boldsymbol{F}(\boldsymbol{x}^{(n)};\Omega) = \boldsymbol{J}(\boldsymbol{x}^{(n)};\Omega)\cdot d\boldsymbol{x}^{(n)}. \tag{A5}$$

The solution coefficients $\hat{\boldsymbol{u}}_{bji}$ in Eq. (12), together with the eigenvalues c_r and ϵ, make up the total number of unknowns $\boldsymbol{x}^{(n)} = [\hat{\boldsymbol{u}}_{bji}, c_r, \epsilon]$ in each iteration and are updated at each step by $\boldsymbol{x}^{(n+1)} = \boldsymbol{x}^{(n)} + d\boldsymbol{x}^{(n)}$ until convergence is reached. When mapping out the solutions in one of the free parameters, e.g., the Reynolds number Re, the vector $\boldsymbol{F} = \boldsymbol{F}(\hat{\boldsymbol{u}}_{bji}, c_r; \mathrm{Re}) = \{F_m\}_{m=1}^{NVAR}$, with

$\boldsymbol{J} = \sum_{k=1}^{NVAR} \partial F_m/\partial x_k$ $(m = 1, \ldots NVAR)$ is the Jacobian matrix where $x = \{x_k\}_{k=1}^{NVAR}$. The aim is to gradually bring the forcing amplitude f_A to zero while increasing the amplitude of the perturbation. A homotopy approach different from the one described above has also been considered. In this method, the already known nonlinear solutions of the BBL flow have been used [18] as an initial guess, with the aim of gradually changing the laminar base Blasius flow to that of the asymptotic suction boundary layer. However, this method has not proven to be successful in the present case.

[1] O. Reynolds, An experimental investigation of the circumstances which determine whether the motion of water shall be direct or sinuous, and of the law of resistance in parallel channels, Philos. Trans. **174**, 935 (1883).

[2] L. Rayleigh, On the stability of certain fluid motions, Proc. Math. Soc. London **11**, 57 (1880).

[3] W. M. F. Orr, The stability or instability of the steady motions of a perfect liquid and of a viscous liquid. Part II: A viscous liquid, Proc. R. Ir. Acad. A **27**, 69 (1907).

[4] A. Sommerfeld, Ein Beitrag zur hydrodynamischen Erklärung der turbulenten Flüssigkeitsbewegung, in *Proceedings of the 4th International Congress Math.* (Rome, 1908), Vol. 3, pp. 116–124.

[5] J. T. Stuart, On the nonlinear mechanics of wave disturbances in stable and unstable parallel flows. Part 1. The basic behavior in plane Poiseuille flow, J. Fluid Mech. **9**, 353 (1960).

[6] E. Hopf, A mathematical example displaying features of turbulence, Commun. Appl. Math. **1**, 303 (1948).

[7] H. Poincaré, Sur le problème des trois corps et les équations de la dynamique, Acta Math. **13**, 1270 (1890).

[8] M. Gutzwiller, Periodic orbits and classical quantization conditions, J. Math. Phys. **12**, 343 (1971).

[9] M. Nagata, Three-dimensional finite-amplitude solutions in plane Couette flow: Bifurcation from infinity, J. Fluid Mech. **217**, 519 (1990).

[10] U. Ehrenstein and M. Rossi, Nonlinear Tollmien-Schlichting waves for a Blasius flow over compliant coatings, Phys. Fluids **8**, 1036 (1996).

[11] H. Faisst and B. Eckhardt, Travelling Waves in Pipe Flow, Phys. Rev. Lett. **91**, 224502 (2003).

[12] H. Wedin and R. Kerswell, Exact coherent structures in pipe flow: Travelling wave solutions, J. Fluid Mech. **508**, 333 (2004).

[13] C. C. T. Pringle and R. R. Kerswell, Asymmetric, Helical and Mirror-Symmetric Traveling Waves in Pipe Flow, Phys. Rev. Lett. **99**, 074502 (2007).

[14] C. Pringle, Y. Duguet, and R. Kerswell, Highly symmetric travelling waves in pipe flow, Philos. Trans. R. Soc. A **367**, 457 (2009).

[15] H. Wedin, A. Bottaro, and M. Nagata, Three-dimensional traveling waves in a square duct, Phys. Rev. E **79**, 065305(R) (2009).

[16] J. F. Gibson, J. Halcrow, and P. Cvitanović, Equilibrium and traveling-wave solutions of plane Couette flow, J. Fluid Mech. **638**, 243 (2009).

[17] D. Wall and M. Nagata, Three-dimensional exact coherent states in rotating channel flow, J. Fluid Mech. **727**, 533 (2013).

[18] H. Wedin, A. Bottaro, A. Hanifi, and G. Zampogna, Unstable flow structures in the Blasius boundary layer, Eur. Phys. J. E **37**, 34 (2014).

[19] J. Jimenez, Coherent structures and dynamical systems, in *Proceedings of the 1987 Summer Program of Center for Turbulence Research (Stanford University, Stanford, CA), Paper No. SEE N88-23086* (Stanford University, Stanford, USA, 1987), pp. 16–34.

[20] B. Hof, C. Doorne, J. Westerweel, F. Nieuwstadt, H. Faisst, B. Eckhardt, H. Wedin, R. Kerswell, and F. Waleffe, Experimental observation of nonlinear traveling waves in turbulent pipe flow, Science **305**, 1594 (2004).

[21] G. Kawahara and S. Kida, Periodic motion embedded in plane Couette turbulence: Regeneration cycle and burst, J. Fluid Mech. **449**, 291 (2001).

[22] Y. Duguet, C. Pringle, and R. Kerswell, Relative periodic orbits in transitional pipe flow, Phys. Fluids **20**, 114102 (2008).

[23] S. Cherubini, P. D. Palma, J. Robinet, and A. Bottaro, Edge states in a boundary layer, Phys. Fluids **23**, 051705 (2011).
[24] Y. Duguet, P. Schlatter, D. S. Henningson, and B. Eckhardt, Self-Sustained Localized Structures in a Boundary-Layer Flow, Phys. Rev. Lett. **108**, 044501 (2012).
[25] G. Chandler and R. Kerswell, Invariant recurrent solutions embedded in a turbulent two-dimensional Kolmogorov flow, J. Fluid Mech. **722**, 554 (2013).
[26] T. Kreilos, G. Veble, T. Schneider, and B. Eckhardt, Edge states for the turbulence transition in the asymptotic suction boundary layer, J. Fluid Mech. **726**, 100 (2013).
[27] T. Khapko, T. Kreilos, P. Schlatter, Y. Duguet, B. Eckhardt, and D. Henningson, Localized edge states in the asymptotic suction boundary layer, J. Fluid Mech. **717**, R6 (2013).
[28] T. Khapko, Y. Duguet, T. Kreilos, P. Schlatter, B. Eckhardt, and D. Henningson, Complexity of localised coherent structures in a boundary-layer flow, Eur. Phys. J. E **37**, 32 (2014).
[29] E. Brand and J. Gibson, A doubly localized equilibrium solution of plane Couette flow, J. Fluid Mech. **750**, R3 (2014).
[30] J. Gibson and E. Brand, Spanwise-localized solutions of planar shear flows, J. Fluid Mech. **745**, 25 (2014).
[31] P. Manneville, Transition to turbulence in wall-bounded flows: Where do we stand? Mech. Eng. Rev. **3**, 15 (2016).
[32] B. Hof, C. W. H. van Doorne, J. Westerweel, and F. T. M. Nieuwstadt, Turbulence Regeneration in Pipe Flow at Moderate Reynolds Numbers, Phys. Rev. Lett. **95**, 214502 (2005).
[33] A. de Lozar, F. Mellibovsky, M. Avila, and B. Hof, Edge State in Pipe Flow Experiments, Phys. Rev. Lett. **108**, 214502 (2012).
[34] A. P. Willis and R. R. Kerswell, Coherent Structures in Localized and Global Pipe Turbulence, Phys. Rev. Lett. **100**, 124501 (2008).
[35] J. Halcrow, J. F. Gibson, P. Cvitanović, and D. Viswanath, Heteroclinic connections in plane Couette flow, J. Fluid Mech. **621**, 365 (2009).
[36] M. Farano, S. Cherubini, J. Robinet, P. De Palma, and T. Schneider, Computing heteroclinic orbits using adjoint-based methods, J. Fluid Mech. **858**, R3 (2019).
[37] G. Kawahara, M. Uhlmann, and L. van Veen, The significance of simple invariant solutions in turbulent flows, Ann. Rev. Fluid Mech. **44**, 203 (2012).
[38] K. Deguchi and P. Hall, Free-stream coherent structures in parallel boundary-layer flows, J. Fluid Mech. **752**, 602 (2014).
[39] H. Wedin, S. Cherubini, and A. Bottaro, Effect of plate permeability on nonlinear stability of the asymptotic suction boundary layer, Phys. Rev. E **92**, 013022 (2015).
[40] H. Wedin and S. Cherubini, Permeability models affecting nonlinear stability in the asymptotic suction boundary layer: The Forchheimer versus the Darcy model, Fluid Dyn. Res. **48**, 061411 (2016).
[41] T. Kreilos, J. Gibson, and T. Schneider, Localized travelling waves in the asymptotic suction boundary layer, J. Fluid Mech. **795**, R3 (2016).
[42] L. Hocking, Non-linear instability of the asymptotic suction velocity profile, Quart. J. Mech. Appl. Math. **28**, 341 (1975).
[43] J. Fransson, Flow control of boundary layers and wakes, Ph.D. thesis, Royal Institute of Technology, KTH Mechanics (2003).
[44] J. Fransson and P. Alfredsson, On the disturbance growth in an asymptotic suction boundary layer, J. Fluid Mech. **482**, 51 (2003).
[45] P. Schmid and D. Henningson, *Stability and Transition in Shear Flows* (Springer, New York, 2001).
[46] F. Pluvinage, A. Kourta, and A. Bottaro, Instabilities in the asymptotic suction boundary layer over a permeable, compliant wall, Phys. Fluids **27**, 054104 (2015).
[47] S. Cherubini, P. D. Palma, and J. Robinet, Nonlinear optimals in the asymptotic suction boundary layer: Transition thresholds and symmetry breaking, Phys. Fluids **27**, 034108 (2015).
[48] O. Levin and D. Henningson, Turbulent spots in the asymptotic suction boundary layer, J. Fluid Mech. **584**, 397 (2007).
[49] P. Schlatter and R. Örlü, Turbulent asymptotic suction boundary layers studied by simulation, J. Phys. **318**, 022020 (2011).

[50] T. Khapko, Transition to turbulence in the asymptotic suction boundary layer, Ph.D. thesis, KTH Royal Institute of Technology (2014).
[51] T. Khapko, P. Schlatter, Y. Duguet, and D. Henningson, Turbulence collapse in a suction boundary layer, J. Fluid Mech. **795**, 356 (2016).
[52] R. Iglisch, Exact Calculation of Laminar Boundary Layer in Longitudinal Flow over a Flat Plate with Homogeneous Suction, Report No. NACA TM 1205 (National Advisory Committee for Aeronautics, Washington, DC, United States, 1949).
[53] C. Gustavsson, Development of three-dimensional disturbances in boundary layers with suction, Master thesis, Luleå University of Technology, Luleå, Sweden, 2000.
[54] P. Forchheimer, Wasserbewegung durch Boden, 45th Edition, Zeitschrift des Vereins deutscher Ingenieure, Düsseldorf, Vol. 45 (1901), p. 1782.
[55] H. F. Burcharth and H. Andersen, On the one-dimensional steady and unsteady porous flow equations, Coastal Eng. **24**, 233 (1995).
[56] S. Whitaker, The Forchheimer equation: A theoretical development, Transp. Porous Media **25**, 27 (1996).
[57] J. Fransson, Investigations of the asymptotic suction boundary layer (Licentiate Thesis), Ph.D. thesis, Royal Institute of Technology, KTH Mechanics (2001).
[58] J. Rotenberry, Finite amplitude steady waves in the Blasius boundary layer, Phys. Fluids A **5**, 1840 (1993).
[59] F. Milinazzo and P. Saffman, Finite-amplitude steady waves in plane viscous shear flows, J. Fluid Mech. **160**, 281 (1985).
[60] R. Verzicco and P. Orlandi, A finite-difference scheme for three-dimensional incompressible flows in cylindrical coordinates, J. Comput. Phys. **123**, 402 (1996).
[61] S. Kline, W. Reynolds, F. Schraub, and P. Runstadler, The structure of turbulent boundary layers, J. Fluid Mech. **30**, 741 (1967).
[62] J. Kim, P. Moin, and R. Moser, Turbulence statistics in fully developed channel flow at low Reynolds number, J. Fluid Mech. **177**, 133 (1987).
[63] M. Chantry, A. P. Willis, and R. R. Kerswell, Genesis of Streamwise-Localized Solutions from Globally Periodic Travelling Waves in Pipe Flow, Phys. Rev. Lett. **112**, 164501 (2014).
[64] R. L. Simpson, The turbulent boundary layer on a porous plate: An experimental study of the fluid dynamics with injection and suction, Ph.D. thesis, Department of Mechanical Engineering, Stanford University (1967).
[65] M. Ferro, B. E. G. Fallenius, and J. H. M. Fransson, On the turbulent boundary layer with wall suction, in *Progress in Turbulence* (Springer, New York, 2017), Vol. VII, pp. 39–41.
[66] J. Jimenez, G. Kawahara, M. Simens, M. Nagata, and M. Shiba, Characterization of near-wall turbulence in terms of equilibrium and "bursting" solutions, Phys. Fluids **17**, 015105 (2005).
[67] F. Waleffe, On a self-sustaining process in shear flows, Phys. Fluids **9**, 883 (1997).
[68] F. Waleffe, Exact coherent structures in channel flow, J. Fluid Mech. **435**, 93 (2001).
[69] F. Waleffe, Homotopy of exact coherent structures in plane shear flows, Phys. Fluids **15**, 1517 (2003).
[70] M. Uhlmann, G. Kawahara, and A. Pinelli, Traveling-waves consistent with turbulence-driven secondary flow in a square duct, Phys. Fluids **22**, 084102 (2010).
[71] W. Rheinboldt and J. V. Burkardt, Algorithm 596: A program for a locally parameterized continuation process, ACM Trans. Math. Softw. **9**, 236 (1983).
[72] W. Rheinboldt and J. V. Burkardt, A locally parameterized continuation process, ACM Trans. Math. Softw. **9**, 215 (1983).